The age-redshift relation for Luminous Red Galaxies in the Sloan Digital Sky Survey

Dan P. Carson[1], Robert C. Nichol[1]

[1] *Institute of Cosmology and Gravitation (ICG), Dennis Sciama Building, Burnaby Road, Portsmouth, PO1 3FX, UK*

16 June 2010

ABSTRACT

We present a detailed analysis of $17,852$ quiescent, Luminous Red Galaxies (LRGs) selected from Sloan Digital Sky Survey (SDSS) Data Release Seven (DR7) spanning a redshift range of $0.0 < z < 0.4$. These galaxies are co-added into four equal bins of velocity dispersion and luminosity to produce high signal–to–noise spectra ($> 100 \mathring{A}^{-1}$), thus facilitating accurate measurements of the standard Lick absorption–line indices. In particular, we have carefully corrected and calibrated these indices onto the commonly used Lick/IDS system, thus allowing us to compare these data with other measurements in the literature, and derive realistic ages, metallicities ($[Z/H]$) and α-element abundance ratios ($[\alpha/Fe]$) for these galaxies using Simple Stellar Population (SSP) models. We use these data to study the relationship of these galaxy parameters with redshift, and find little evidence for evolution in metallicity or α–elements (especially for our intermediate mass samples). This demonstrates that our subsamples are consistent with pure passive evolving (i.e. no chemical evolution) and represent a homogeneous population over this redshift range. We also present the age–redshift relation for these LRGs and clearly see a decrease in their age with redshift ($\simeq 5$Gyrs over the redshift range studied here) which is fully consistent with the cosmological lookback times in a concordance ΛCDM universe. We also see that our most massive sample of LRGs is the youngest compared to the lower mass galaxies. We provide these data now to help future cosmological and galaxy evolution studies of LRGs, and provide in the appendices of this paper the required methodology and information to calibrate SDSS spectra onto the Lick/IDS system.

Key words: methods: observational – galaxies:elliptical – galaxies:abundances – galaxies:evolution – galaxies: fundamental parameters

1 INTRODUCTION

The formation and evolution of massive elliptical (passive) galaxies in the Universe is interesting for both studies of galaxy evolution and cosmology. In the former case, such galaxies present an observational challenge for hierarchical models of structure formation, as some form of feedback is required to suppress on-going star formation in such massive systems (see Wake et al. (2006) and references therein). For cosmology, such massive ellipticals can be used to directly constrain cosmological parameters (e.g., as standard candles; Collins & Mann (1998)) and provide efficient tracers of the Large Scale Structure (LSS) in the Universe (Eisenstein et al. 2001). Moreover, the (relative) ages of massive ellipticals, as a function of redshift, offers the possibility of directly constraining the Hubble parameter, thus providing vital information on the expansion history of the Universe and therefore, the equation of state of dark energy (see **?** for a discussion of the underlying concept, and Jimenez et al. (2003); Simon et al. (2005) and Stern et al. (2009) for observational constraints obtained from using this technique).

In this paper, we revisit the techniques used to constrain cosmological parameters through the age–redshift relationship of passive (elliptical), massive galaxies. In detail, we present a new analysis of the ages of Luminous Red Galaxies (LRGs; Eisenstein et al. (2001)), as selected from the Sloan Digital Sky Survey (SDSS; York et al. (2000)). The key difference present herein compared to other such work with SDSS spectral data (e.g. Bernardi et al. (2003a,b); Eisenstein et al. (2003); Bernardi et al. (2006)) is that we calibrate, for the first time, the SDSS spectra onto the well-known, and well-studied, Lick/IDS system (Burstein et al. (1984); Worthey et al. (1994)), thus allowing us to exploit a host of previous work on this system including the Simple Stellar Population (SSP) modeling in the literature

(Worthey (1998); Maraston (1998); Korn et al. (2005)) and comparisons with Lick measurements in the literature. In a companion paper, we will use the age–redshift data derived for SDSS LRGs in this paper to obtain cosmological constraints.

In Section 2 of this paper, we outline the SDSS galaxy data we use to construct our age–redshift relation, specifically luminous (massive), quiescent galaxies. We also discuss the stellar data available to calibrate these galaxies onto the Lick/IDS system (see also Appendix A). In Section 3, we provide details about the SSP models we have used to determine the ages, metallicities and α–enhancements of our galaxies, using a Markov Chain Monte Carlo (MCMC) technique for parameter estimation. We discuss our results in Section 4, including the effect of priors, and conclude in Section 5. Appendix A provides the extensive details on how we calibrate the SDSS spectra onto the Lick/IDS system, including all the necessary corrections made to the data. In Appendix B, we provide a review of tests we have performed to quantify the robustness of our spectral measurements, including comparisons with data from the literature. We assume a concordance, flat ΛCDM cosmology, with $h = 0.7$ and $\Lambda = 0.7$, where required.

2   SAMPLE SELECTION

The Sloan Digital Sky Survey (SDSS; York et al. 2000; Stoughton et al. 2002; Abazajian et al. 2003) is a photometric and spectroscopic survey, covering $\simeq 8000 \mathrm{deg}^2$ of the northern sky, using a 2.5 meter telescope at Apache Point Observatory in New Mexico, USA. The photometric survey consists of simultaneous observations of the sky using 5 optical filters (u, g, r, i and z), providing a database of hundreds of millions of detected objects all with accurate photometric and astrometric calibrations (Pier et al. 2003; Lupton et al. 2001; Hogg et al. 2001).

The SDSS spectroscopic galaxy survey consists of two samples of galaxies selected using different criteria; namely the MAIN sample (Strauss et al. 2002) and the LRG sample (Eisenstein et al. 2001). The SDSS spectra of these galaxies span a wavelength range of $3800 < \lambda < 9200$Å with a median resolution of R ~ 1800 (R $\equiv \lambda/\Delta\lambda$), which is approximately 3 Å (although this varies as a function of wavelength and is different for each fiber). The SDSS spectra are automatically reduced using dedicated software, which flux calibrates the spectra and references them to the heliocentric frame and converts to vacuum wavelengths. The software also measures a redshift for each object and measures a series of spectral features consistent (in their wavelength definitions) as the standard Lick indices (see Section 2.2), but are not calibrated onto the Lick systems as no attempt has been made to match to the resolution of the Lick/IDS system.

For the analysis presented in this paper, we do not use the Lick indices measurements from the standard SDSS pipeline, but instead determine our own line-strengths after matching the instrumental resolutions (see Section A). However, we do use redshifts (z), velocity dispersions (`velDisp`), magnitudes (u,g,r,i,z) and other derived quantities such as the r-band de Vaucouleurs radii (`deVRad_r`) and the r-band de Vaucouleurs profile axis ratio (`deVAB_r`) from the standard SDSS spectral pipeline, made available through

the Catalog Archive Server (CAS)[1]. The spectral data used in this paper was obtained from the Data Archive Server (DAS)[2].

2.1   SDSS Luminous Red Galaxies

For our analysis, we only used Cut I Luminous Red Galaxies (LRGs) as outlined in (Eisenstein et al. 2001). This is achieved by selecting objects from CAS using the `TARGET_GALAXY_RED` flag, thus yielding a pseudo volume-limited sample of LRGs between $0.15 < z < 0.35$. Below $z = 0.15$ contamination by low redshift star-forming galaxies increases the space density of galaxies that satisfy the SDSS LRG colour-colour selection, while above $z = 0.35$ the space density of SDSS LRGs decreases due to the 4000 Å break dropping out of the SDSS g-band. We do not use the Cut II LRG sample at $z > 0.4$ as we require velocity dispersion measurements for each object and these are not supplied above this redshift. Therefore, we impose an upper redshift limit of $z = 0.4$ in our sample and analysis.

We further restrict our sample to only include LRGs with `specClass EQ 'SPEC_GALAXY'` (spectrum classified as a galaxy), `zStat EQ 'XCORR_HIC'` (redshift obtained from cross-correlation with a template), `zWarning EQ 0` (no warning flags on the redshift), `eClass < 0` (indicates an old stellar population), `z < 0.4` (redshift less than 0.4) and `fracDev_r > 0.8` (indicating a surface brightness profile best fit by a de Vaucouleurs profile). Based upon these selection criteria, we obtain a sample of approximately $77,000$ LRGs (see Figure 2 for the redshift distribution of this sample).
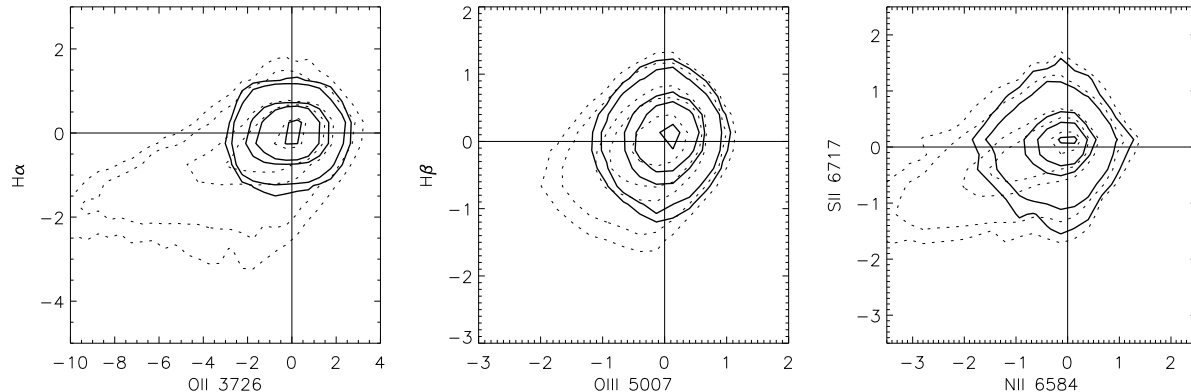
2.1.1   Quiescent Galaxies

At low redshift, our sample will be contaminated by bulges in late-type galaxies due to the fiber size ($3''$) of the SDSS spectrographs. To reduce this contamination, and increase the number of truly quiescent galaxies in our sample, we make further cuts based on the emission line properties of our LRG sample, e.g., we use standard emission lines such as Hα, Hβ and [O III]$\lambda 5007$ (Fukugita et al. 2004; Zhao et al. 2006; Roseboom et al. 2006). If left unchecked, such nebular emission, or emission associated with low-ionization nuclear emission-line region (LINER) activity, would confuse our interpretation of the SSP parameters derived from these objects.

To combat this, we use the MPA-JHU spectral line data[3] to select only those objects that are consistent with zero emission. In their original work, Tremonti et al. (2004) fitted the spectral energy distributions (SEDs) of Bruzual & Charlot (2003) to the SDSS galaxy spectra in Data Release Four (DR4), subtracted off the best fitting SED, and then measured the line-strengths of [O II]$\lambda_{air}3726$, Hβ , [O III]$\lambda_{air}5007$, [N II]$\lambda_{air}6584$, Hα and [S II]$\lambda_{air}6717$. This SED fitting approach has now been applied to the SDSS Data Release Seven (DR7) dataset using

---

[1] http://www.sdss.org/dr7/access/index.html#CAS
[2] http://www.sdss.org/dr7/access/index.html#DAS
[3] http://www.mpa-garching.mpg.de/SDSS/DR7/raw_data.html

Figure 1. Distribution of the line-strengths from the MPA-JHU dataset for the LRGs of our sample. Dotted contours show the full LRG sample while solid lines show the quiescent sample selected based on their Hα and [O II] line-strengths. While only two lines have been used in the production of the quiescent sample, all lines show distributions consistent with zero-emission.

the stellar population synthesis spectra of Charlot & Bruzual (2008). We use this latest DR7 dataset herein.

In an approach similar to Yan et al. (2006) we fit a two component function to the line-strength distributions of Tremonti et al., that consists of a normal component to describe the quiescent LRGs, plus a log-normal component to describe the active objects. The best fit is then used to determine the small zero-point offsets that exist in the dataset of Tremonti et al. from which we then select objects that are consistent with zero emission, at the 2σ level, in Hα and [O II], hence removing the need to make corrections to the Lick index line-strengths for the possible presence of nebular emission. With these constraints on the emission-line characteristics of the LRG sample, we obtain approximately $35,000$ galaxies that we refer to as the quiescent LRG sample.

While it is possible to use different, and more, emission lines in determining the quiescent sample, doing so results in a significant reduction of our sample size. For instance, including Hβ and [O III] in the joint constraint with Hα and [O II] yields approximately $28,000$ LRGs over $0.0 < z < 0.4$ and further inclusion of [N II] and [S II] constraints yields approximately $19,000$ objects. While the more restrictive sample selection ensures a more quiescent sample, the reduction in the total number of objects available hampers our ability to explore the evolution of the SSP parameters over the desired redshift range. But, even selecting on Hα and [O II] alone helps to ensure that we are not including objects with significant emission in Hβ as show in Figure 1. In Figure 2 we also show the redshift distribution of the quiescent LRGs sample.

2.1.2 Further Selection Criteria

In order to select the same population of objects over the redshift range $0.0 < z < 0.4$ we need to select on physical properties such as velocity dispersion and absolute luminosity. Aperture corrections are applied to the SDSS velocity dispersion measurements following the approaches of Jørgensen et al. (1995) and Bernardi et al. (2003a), see Section A5. To select on luminosity we have performed K-corrections using the code *kcorrect* code of
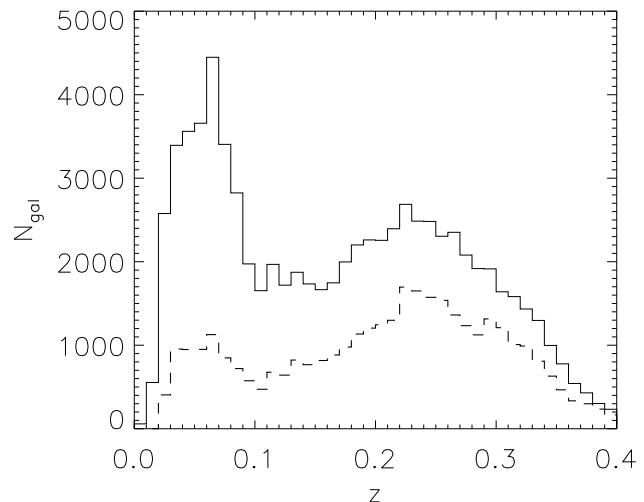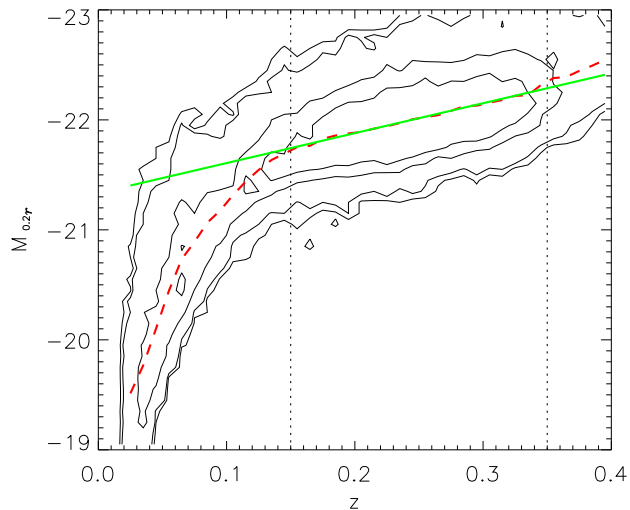

Figure 2. Redshift distribution of our LRG sample (solid line) and our quiescent sample (dashed line).

Blanton & Roweis (2007) and have K-corrected all galaxies to a redshift of 0.2 (the median of our distribution) in order to minimise errors in these K-corrections.

We have modeled the luminosity evolution in our LRGs using a simple linear fit to the volume limited part of the K-corrected, magnitude-redshift distribution and then extrapolated this to higher and lower redshifts, see Figure 3. From this, we obtain an evolutionary (e) correction which we apply to our quiescent LRG sample. A more detailed approach to determine the evolution correction using stellar population synthesis models is unlikely to significantly improve the accuracy of the e-correction given the difficulty that current models have in explaining the evolution of the SDSS LRGs colours (Wake et al. 2006; Maraston et al. 2009).

When reporting absolute magnitudes, we will use the notation $M_{0.2_r}$ to denote r-band SDSS magnitudes that have been K+e corrected such that the r-band has been shifted to $z = 0.2$.

After correcting velocity dispersions for aperture effects and performing K+e corrections to the magnitudes, we have

Figure 3. Distribution of our quiescent LRG sample in the redshift-luminosity plane, with a simple linear model (green/solid line) used to describe the luminosity evolution of the LRGs. Contours show the distribution in number density of the whole sample, and are in the intervals 5,10,50,100. The region bounded by the vertical dotted lines represent the volume-limited portion of our sample and the (red/dashed line) shows the median luminosity in redshift intervals of $\Delta z = 0.01$.

produced four subsamples of quiescent LRGs (see Table 2 for numbers in each sample). These subsamples span an intervals of $\Delta M_{0.2_r} = 0.6$ and $\Delta\sigma_v = 30\,\mathrm{km\,s^{-1}}$ and are shown as the boxed regions in Figure 4. Objects satisfying these criteria are then co-added to produce high signal-to-noise spectra after binning into redshift intervals of $\Delta z = 0.02$. This redshift interval is small enough that there is little evolution in the ages of the objects within the bin such that we are co-adding objects of sufficiently similar ages, e.g. in the case of a concordance cosmology the age evolution within a bin is approximately 0.2 Gyr over the redshift range $0.0 < z < 0.4$, and is big enough to yield a sufficient number of objects to reach S/N levels of approximately 100 Å $^{-1}$

In generating the co-added spectrum we have adopted an approach similar to Bernardi et al. (2006). Briefly, after binning our sample in redshift, absolute magnitude and velocity dispersion we shift each spectrum to its restframe. All spectra in a given bin are normalised to the median flux in the region $4500 - 5500$ Å and combined pixel-by-pixel using a weighted arithmetic mean where the weights are determined by the inverse variance of the flux in each pixel. This approach means that not all spectra contribute equally to the co-added spectrum but it does mean that those pixels contaminated by residuals from imperfect sky-subtraction contribute less to the final stacked spectrum.

2.2 Lick/IDS System

A long term programme undertaken by Burstein et al. (1984); Faber et al. (1985); Worthey et al. (1994) and Trager et al. (1998), amongst others, has yielded a library of stellar spectra, obtained with the Image Dissector Scanner (IDS, Robinson & Wampler 1972) on the Shane 3m telescope at the Lick Observatory. These authors have also es-

tablished a spectral index system used to investigate element abundances from low-resolution integrated spectra of extra-galactic stellar populations.

Twenty five absorption features in the wavelength range $4000 < \lambda < 6000$ Å at ~ 9 Å resolution, have been identified that are sensitive to effective temperature (T_{eff}), surface gravity (g) and metallicity (Z) of a star. The wavelength definitions of these features were chosen such that the broad absorption features found in elliptical galaxies could be studied and to minimise the effect of galaxy velocity dispersion on the measured line-strengths.

All features measured on the Lick/IDS system are defined by a central "feature" bandpass and two adjacent "pseudocontinuum" bandpasses, see Appendix A. From this continuum and feature it is possible to measure a "pseudo" equivalent width (EW). It is not a true EW as the wavelength definitions for the bandpasses are fixed and, depending on the element abundances, instrumental resolution or velocity dispersion of the stellar population, the wings of an absorption feature may extend beyond the feature bandpass.

As a consequence of adopting fixed wavelengths to determine the continuum and feature fluxes, the measured line-strength depends on the flux in the continua bandpasses as well as the feature bandpass. The continua also contain absorption features which, when coupled to the effects of galaxy velocity dispersions and instrumental resolution, will help suppress its average flux.

Other factors that effect the measured line-strength of absorption features are gas, dust and telluric features. Although dust has little effect due to the generally narrow nature of the features, gas can be a problem. Nebular emission will contaminate the measured line-strength of the Balmer lines by filling in the "natural" absorption (Moore et al. 2002, and references therein) and, when using the Hβ absorption index, will lead to incorrectly determining older ages for stellar populations. While the Hβ index line-strength is directly affected by Balmer emission from ionized gas, some indices are indirectly affected by emission, e.g. the red sideband of Mg b can be contaminated by [N I] (Goudfrooij & Emsellem 1996).

Telluric emission and absorption can also have a significant impact on the accuracy of the measured line-strengths, but stacking spectra in order to improve the S/N of the Lick indices also allows us to minimise the impact from these telluric features. By co-adding spectra at different redshifts, telluric features "appear" at different restframe wavelengths in the deredshifted spectra. Using the inverse variance of the flux when weighting each pixel allows us to minimise the impact from these features on the final stacked spectrum.

It should be noted that the SDSS convention is to present all wavelengths as vacuum wavelengths. Therefore, the wavelength definitions of all Lick Indices were converted to vacuum wavelengths (Morton 1991) prior to performing any measurements of index line-strengths on spectra. We have used the publicly–available software IN-DEXF[4] (Cardiel 2007) to measure our absorption feature line-strengths from our co-added stacked LRG spectra.

---

[4] http://www.ucm.es/info/Astrof/software/indexf/indexf.html
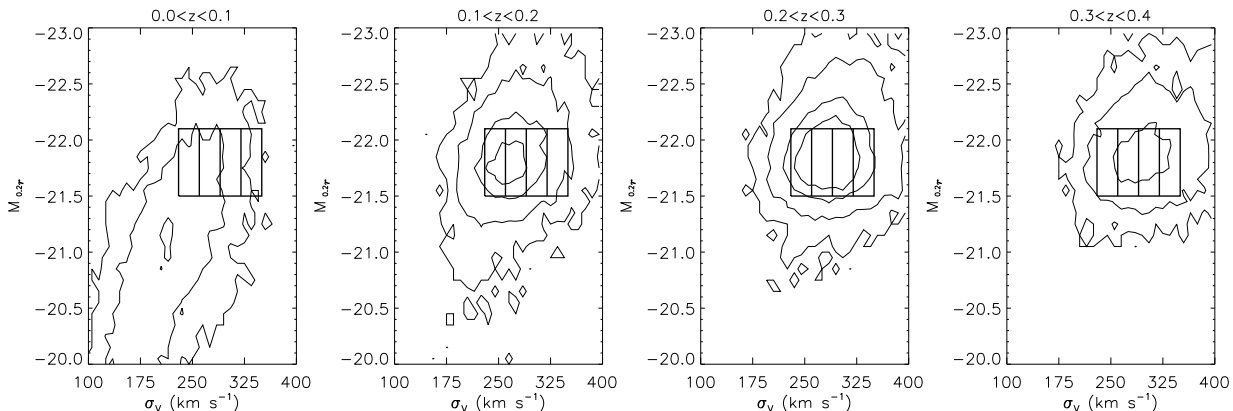
Figure 4. Distribution of our quiescent LRG sample in the velocity dispersion-luminosity plane in four different redshift slice of $\Delta z = 0.1$ over the redshift range $0.0 < z < 0.4$. Velocity dispersions have been aperture corrected and absolute magnitudes have been k+e corrected to $z = 0.2$. Contours show the distribution in number density of the whole sample, and are in the intervals 1,10,50,100. The four boxes are the same in each panel and show the boundaries used to create the four mass (velocity dispersion) samples used in Section 4 when exploring the redshift evolution of the SSP parameters for the quiescent sample.

2.3 Lick Stars in the SDSS

To properly calibrate to the Lick/IDS system it is necessary to have SDSS observations of Lick stars, or galaxies, to allow the zero-point offsets to be determined, see Appendix A1. The library of Lick stars that could be used in calibrating the SDSS to the Lick system have not been intentionally targeted by the SDSS and therefore requires serendipitous observations of Lick stars to allow the SDSS to be placed on the Lick system.

The diameter of the SDSS fibres is $3.0''$ with the median seeing at Apache Point of $\sim 1.5''$. We have therefore chosen a cut-off of $< 1.5''$ when matching SDSS objects and Lick star coordinates. In searching for Lick stars in the SDSS we have included both *special* and *survey* plates in the search and have identified 13 stars from the Lick library that match SDSS objects to within $1.5''$; 11 stars in M67 (*special plate* # 0321) and 2 stars in NGC 7789 (*special plate* # 2377) and are listed in Table 1. The cluster proper motion dispersion for M67 is $\sim 0.8 \, \mathrm{mas \, yr^{-1}}$ (McNamara & Sanders 1978) and for NGC 7789 is $\sim 0.4 \, \mathrm{mas \, yr^{-1}}$ (McNamara & Solomon 1981), with only one star in Table 1 having a measured proper motion of $\sim 9.0 \, \mathrm{mas \, yr^{-1}}$ for M67 F 164 (Hog et al. 1998). Given the small size of the proper motions we have ignored this effect when matching the coordinates of SDSS objects to the Lick stars in these two clusters.

The details of how our SDSS LRG spectra were calibrated onto the Lick/IDS system using the Lick stars in Table 1 is given in Appendix A.

3 METHOD

3.1 Simple Stellar Population Models

Simple stellar population (SSP) models have become an invaluable tool in allowing the physical properties of stellar populations to be probed via measurements of absorption features in their integrated spectra. But absorption features generally suffer from the same age-metallicity degeneracy that effects the interpretation of star formation histories and chemical evolution of stellar population using their broad-

Table 1. Lick stars observed by SDSS

Star	Plate	MJD	FiberID	Spectral Type
M67 IV-77	0321	51612	385	K0 IV
M67 IV-68	0321	51612	386	G8 V
M67 I-17	0321	51612	388	F0 V
M67 F 115	0321	51612	463	F6
M67 F 105	0321	51612	466	K2 III
M67 F 231	0321	51612	479	K0 III
M67 II-22	0321	51612	480	K0 IV
M67 F 175	0321	51612	490	-
M67 F 164	0321	51612	491	K1 III
M67 IV-20	0321	51612	499	K0 III/IV
M67 F 193	0321	51612	519	K0 IV
NGC 7789 676	2377	53756	160	G8 III
NGC 7789 897	2377	53756	492	G9 III

Note: Spectral classifications obtained from SIMBAD

band optical colours. Balmer lines become weaker while metallic line become stronger as the age and metallicity of a stellar population increases.

While different absorption features behave differently to age and metallicity, with some more sensitive to age and others to metallicity, a further complication is that due to α-enhancement. Worthey (1998) has shown that regardless of isochrones, stellar library, fitting functions or authors, the SSP models at the time were unable to explain the large spread in Mg at fixed Fe of ellipticals. This overabundance of Mg is considered to be a consequence of the different timescales involved in the evolution of stars of different masses. The abundance of the α-elements (O, Ne, Mg, Si amongst others), which are primarily a product of nucleosynthesis in Type II supernovae, is enhanced over the the abundance of the Fe-peak elements (Fe, Cr amongst others) that result from Type Ia supernovae. The ages and metallicities derived for SSPs differ depending on whether an α-element or Fe-peak element is used to represent metallicity ([Z/H]).

Since elliptical galaxies show an enhancement of α-element over Fe-element abundance, it has become necessary

to employ SSP models that account for these effects. In this work we use the SSP models of Korn et al. (2005, hereafter KMT05) which use the Evolutionary Population Synthesis (EPS) scheme of Maraston (1998, hereafter M98) and the method of Thomas et al. (2003, hereafter TMB03) to produce the line-strengths of the Lick indices for stellar populations with variable element abundance. In KMT05, the authors use model stellar atmospheres to produce synthetic stellar spectra from which they compute line-strengths and from this, index response functions as a function of metallicity. They then use the scheme of TMB03 to produce Lick index line-strengths that account for variable $[\alpha/\text{Fe}]$ ratios. These models have been calibrated on globular clusters that are known to have enhanced $[\alpha/\text{Fe}]$ ratios above the solar value.

3.2 Markov chain Monte Carlo

Different authors have employed different strategies when converting between the observed line-strengths in galaxy spectra and the model parameters (Mehlert et al. 2003; de la Rosa et al. 2007). However, most previous techniques have involved interpolating a grid of model index values at the location of the observed index values for the object in question. Since the KMT05 models have three SSP parameters, this requires that one of the parameters needs to be fixed and there is normally an iterative procedure employed to explore the parameter space. At each iteration, a new set of model grids are generated and the observed index values are used to re-generate the appropriate SSP parameters. In order to determine the correct SSP parameters for the observed index line-strengths, multiple model index grids may be used. Moreover, each author may have a different convergence criteria for these iterations such that the same SSP parameters need to be reproduced with different index-index grids and are consistent to a pre-determined level.

In this work, we explore an alternative methodology, which is based on a Markov chain Monte Carlo (MCMC) technique to perform the iterative minimisation in order to obtain the SSP parameters that correspond to the measured index line-strengths of the object under study. In the context of Bayesian inference, the MCMC process produces a random sequence of dependent variables that are drawn directly from the posterior distribution which is achieved using Bayes' Theorem:

$$p(\boldsymbol{\theta}|y) = \frac{p(y|\boldsymbol{\theta})p(\boldsymbol{\theta})}{\int p(y|\boldsymbol{\theta})p(\boldsymbol{\theta})d\boldsymbol{\theta}} \quad , \tag{1}$$

where $p(\boldsymbol{\theta}|y)$ is the posterior probability density and assigns a probability to the model, $\boldsymbol{\theta}$, given the data, y, and any prior knowledge concerning the model. The probability density $p(y|\boldsymbol{\theta})$ is associated with obtaining the data given the vector of model parameters and is also called the likelihood ($\mathcal{L}$). The marginal probability density, $p(\boldsymbol{\theta})$, describes the probability associated with the parameter vector and encompasses any prior knowledge of the model parameters. The denominator in the above expression can be considered a normalisation factor and is ignored in our implementation.

We implement the Metropolis-Hastings algorithm (Metropolis et al. 1953; Hastings 1970) to ensure that the stationary distribution of the Markov chain samples from the posterior distribution. This form of MCMC uses a candidate generating, or proposal, distribution to propose new locations in parameter space which allows the likelihood surface to be explored. During this exploration the proposed new locations are accepted or rejected based on logical criteria embodied in the Metropolis-Hastings algorithm.

While the form of the candidate-generating distribution does not impact on the ability of the Metropolis-Hastings algorithm to reach a stationary distribution, it does impact on the efficiency of the convergence to stationarity (Doran & Müller 2004). The most efficient candidate-generating distribution to adopt would be that of the posterior distribution, but this is not known a priori. In our implementation we adopt a multivariate normal distribution as our candidate-generating distribution and estimate the covariance matrix from the data itself.

Convergence to the stationary distribution is identified through use of the Gelman-Rubin $\widehat{\mathcal{R}}$-statistic (Gelman & Rubin 1992) with convergence identified when $\widehat{\mathcal{R}} \leqslant 1.1$ (Verde et al. 2003) for each parameter of the model. Identifying convergence allows the "burn-in" phase to be excluded from the chain and accurate estimation of the confidence-intervals on the model parameters.

3.3 Likelihood Estimation

In order to use the SSP models of KMT05 with our MCMC approach we adopt a trilinear interpolation scheme, since the models have three parameters (age, metallicity and α-iron ratio), such that the SSP models can be investigated at an arbitrary location in parameter space. While there is a unique mapping from model parameters to index values, there is no unique mapping from index values to model parameters and therefore the models cannot be inverted. We must therefore use multiple Lick indices simultaneously in order to break this degeneracy.

The Metropolis-Hastings algorithm employs a likelihood ratio test in order to determine acceptance or not of a candidate position in parameter space. The likelihood ($\mathcal{L} \equiv p(y|\boldsymbol{\theta})$) is obtained by assuming that the data, y, is a set of N independent normally distributed random variables, $y_i, i = 1, \ldots, N$ (Cowan 1998). Each y_i has a different and unknown mean, μ_i, but known variance, σ_i^2. The joint p.d.f. is the product of these N normal distributions:

$$\mathcal{L} = \prod_{i=1}^{N} \frac{1}{\sqrt{2\pi}\sigma_i} \exp\left(\frac{-(y_i - \mu_i)^2}{2\sigma_i^2}\right) , \tag{2}$$

where the true values, μ_i, depend on the model parameters, i.e. $\boldsymbol{\theta} = (\theta_1, \ldots, \theta_m)$. Taking the logarithm of the joint p.d.f. yields

$$\ln \mathcal{L}(\boldsymbol{\theta}) = \sum_{i=1}^{N} \frac{1}{\sqrt{2\pi}\sigma_i} - \frac{1}{2} \sum_{i=1}^{N} \frac{(y_i - \mu_i(\boldsymbol{\theta}))^2}{\sigma_i^2} . \tag{3}$$

We can maximise the log-likelihood by minimizing the χ^2 function,

$$\chi^2(\boldsymbol{\theta}) = \sum_{i=1}^{N} \frac{(y_i - \mu_i(\boldsymbol{\theta}))^2}{\sigma_i^2} \ . \tag{4}$$

In the context of estimating SSP parameters from line-strength data, $y_i \pm \sigma_i \equiv I_i \pm d\,I_i$, where I_i is the line-strength of a particular absorption feature, $d\,I_i$ is its one-sigma error and i represents the Lick index used, e.g. Hβ , Mg b etc. The "true" absorption indices, μ_i, are determined from interpolating the SSP models of KMT05 for a particular set of model parameters, $\boldsymbol{\theta} = \{t, [\text{Z/H}], [\alpha/\text{Fe}]\}$.

At each location in parameter space, we use the SSP models to determine the corresponding values for the chosen Lick indices using the the trilinear interpolation method to go from model parameters to Lick index line-strengths. The MCMC approach is then used to iteratively maximise the likelihood, such that at each stage in the evolution of the chain, the likelihood, $\mathcal{L}_{n+1}$, calculated at the new candidate position, $\boldsymbol{\theta}_{n+1}$, is compared with the likelihood, $\mathcal{L}_n$, determined at the present location in parameter space, $\boldsymbol{\theta}_n$. The Metropolis-Hastings algorithm is then used to make the decision on accepting or rejecting the candidate position. If the next step is rejected then the current step is re-saved as part of the chain.

The chain now performs a random walk in parameter space and generates the sequence of parameter samples $\{\boldsymbol{\theta}_1, \boldsymbol{\theta}_2, \ldots, \boldsymbol{\theta}_n, \boldsymbol{\theta}_{n+1}\}$. Once the chain has converged to the stationary distribution, i.e. burned in, the random walk will be confined to the vicinity of the global mode in the posterior distribution. In Appendix B we test this method of SSP parameter estimation by comparing with previously published results from Thomas et al. (2005, hereafter TMBO).

4 RESULTS

4.1 Line Strengths

The relationship between the line-strength and redshift for the four different mass (velocity dispersion) samples, defined in Figure 4, are presented in Figure 5 for a selection of the key Lick indices used in age-dating of galaxy spectra (again see Appendix for details of how the SDSS spectra were calibrated onto the Lick system). These relationships are consistent with that of a passively evolving stellar population, i.e. the strength of Hβ and HγF indices increase with redshift while the Mg b and $\langle$Fe$\rangle$ lines decrease in strength, indicated by the dotted line in each panel.

The scatter in these relationships is consistent with the error on a typical line-strength and there is a clear trend with velocity dispersion, i.e. Mg b and $\langle$Fe$\rangle$ show a positive correlation with velocity dispersion while HγF shows a negative correlation. These trends are consistent with the finding from other authors, e.g. Bender et al. (1993); Kuntschner et al. (2001); Bernardi et al. (2003b); Loubser et al. (2009). While there is no obvious segregation of the Hβ-redshift relationships there is a hint that the $260 < \sigma_v \leqslant 290$ km s^{-1} (circles/green) sample yields line-strengths that are systematically larger than the $320 < \sigma_v \leqslant 350$ km s^{-1} (diamonds/pink) sample, consistent with the negative correlation observed by other studies.

### 4.2 SSP Parameter Estimates - Uniform Priors

Using the HγF, Mg b and $\langle$Fe$\rangle$ data in Figure 5 and the parameter estimation method outlined in Section 3 we determine the SSP parameters for each mass sample and the results are shown in Figure 6. These parameter estimates have been obtained using uniform priors that cover the full parameter space of the KMT05 models, i.e. age (Gyr) $\sim \mathcal{U}(0.31, 18.2)$, [Z/H] $\sim \mathcal{U}(-1.0, 0.97)$, [$\alpha$/Fe] $\sim \mathcal{U}(-0.25, 0.73)$, when computing the posterior probability using Equation 1, and then estimating the 16, 50 and 84 percentiles from the posterior distribution for each parameter after marginalising over the remaining parameters. In the rest of this paper, the median is used to define the "location" and the 16 and 84 percentiles the 1σ error on SSP parameters.

The evolution in [α/Fe] with redshift is somewhat confusing as the low (blue triangles) and high (pink diamonds) mass (velocity dispersion) samples exhibiting significant scatter and may not be consistent with a constant value over the entire redshift range (there is some indication for a change in behaviour at $z > 0.35$). The intermediate mass samples (green circles and red squares) are more stable and exhibit no significant gradient, as expected for galaxies that are not chemically evolving. There does however appear to be a positive correlation between velocity dispersion and [α/Fe] which is consistent with other studies, e.g. Thomas et al. (2005).

The evolution in [Z/H] with redshift is also consistent with a chemically unevolving population of objects, although the lowest mass sample does exhibit a significant gradient. The metallicity also exhibits a significant positive correlation with velocity dispersion, where the more massive objects have higher metallicity, again consistent with other studies. Finally, the evolution in *age* with redshift exhibits the expected behavior; galaxies become younger with redshift, with a trend that suggests the most massive objects are, in fact, the youngest.

While the Hβ and HγF trends are consistent with tracing a passively evolving population, it is not possible to obtain consistent estimates of the SSP parameters using these indices. The dotted line in Figure 5 is the relationship expected for a population of objects in a ΛCDM concordance cosmology, with $[Z/H] = 0.37$ and $[\alpha/Fe] = 0.27$ and a formation age of 4.5 Gyr. To reproduce the Hβ line-strengths, a population with the same chemical composition would need a formation age of approximately 2.5 Gyr and hence yield inconsistent line-strengths for Hγ.

In Figure 7 we show the correlations between the parameter estimates of Figure 6 and in Table 2 we show the Spearman rank correlation coefficient ($-1 \leqslant \rho \leqslant +1$) and in brackets the significance of the correlation from zero ($0 \leqslant s_\rho \leqslant 1$; with low values having greater significance). From this we can see that, except for the lowest mass sample, correlations between the parameters have little statistical significance, i.e. values for $s_\rho > 0.1$. While interpretation of the lowest mass sample is difficult because of the gradients in [Z/H] and [α/Fe] with redshift, possibly due to including a population of young objects at low redshift (c.f. the Hβ redshift relationship in Figure 5), there does appear to be a significant correlation between the chemical composition of
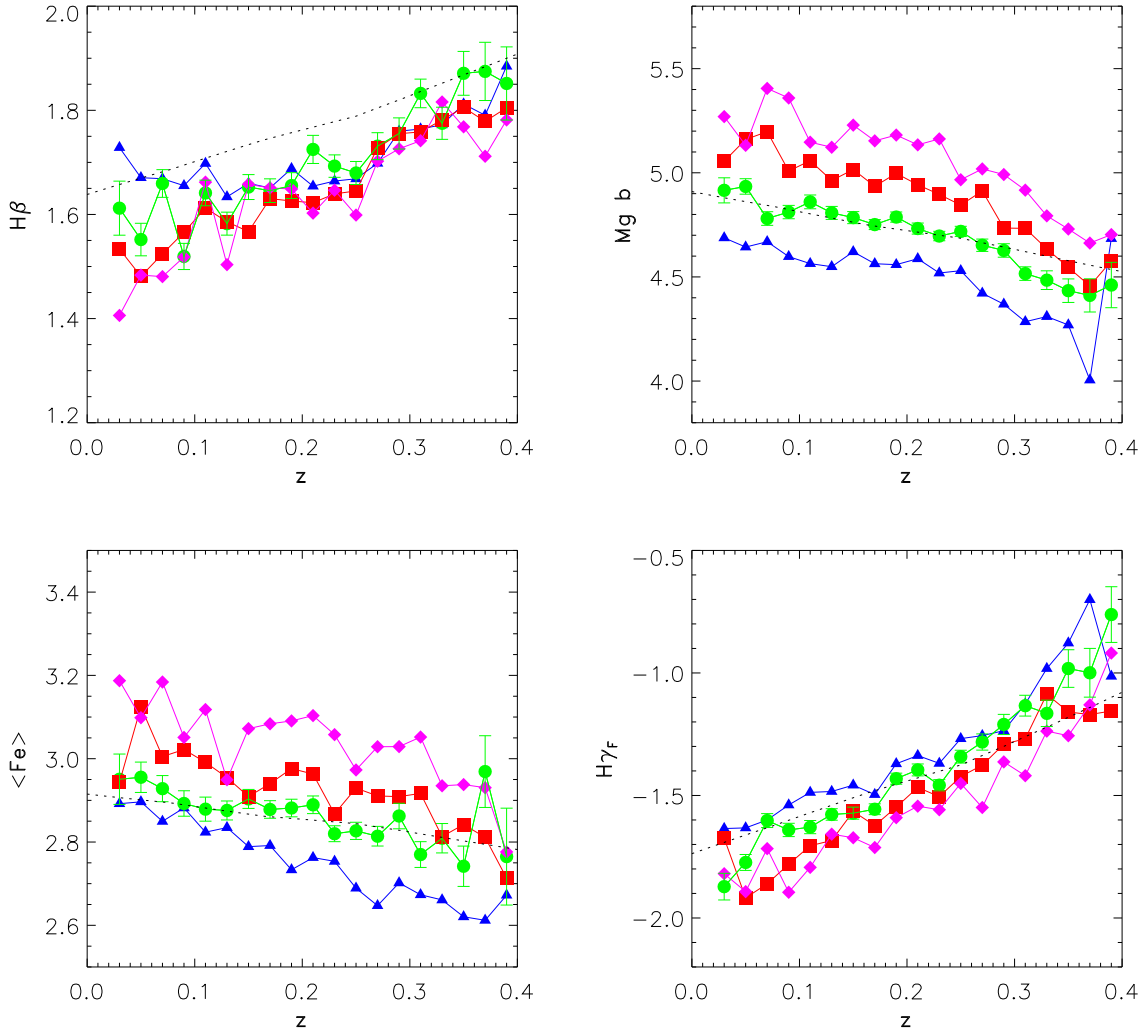
Figure 5. Line-strengths of Hβ, Mg b , $\langle$Fe$\rangle$ and HγF as a function of redshift for the four samples of Figure 3; $230 < \sigma_v \leqslant 260\,\mathrm{km\,s^{-1}}$ (blue triangles), $260 < \sigma_v \leqslant 290\,\mathrm{km\,s^{-1}}$ (green circles), $290 < \sigma_v \leqslant 320\,\mathrm{km\,s^{-1}}$ (red squares), $320 < \sigma_v \leqslant 350\,\mathrm{km\,s^{-1}}$ (pink diamonds). The dotted line shows the expected variation in the line-strengths for an object with $[Z/H] = 0.37$ and $[\alpha/Fe] = 0.27$ and a formation age of 4.5 Gyr for a ΛCDM cosmology. Segregation of the line-strengths for the different samples is obvious except in the case of Hβ. The more massive the sample (i.e. the higher velocity dispersion), the stronger the Mg b and $\langle$Fe$\rangle$ line-strengths and the weaker the HγF line-strength at a given redshift. Errors are only provided on the the $260 < \sigma_v \leqslant 290\,\mathrm{km\,s^{-1}}$ sample (green circles) to avoid overcrowding on the plot. The errors on the other relations are similar as they have comparable signal-to-noise.

Table 2. SSP parameter correlations

Sample	Total Number	t–[Z/H]		t–[α/Fe]		[α/Fe]–[Z/H]	
$230 < \sigma_v \leqslant 260\,\mathrm{km\,s^{-1}}$	4472	0.54	(0.05)	-0.71	(0.01)	-0.64	(0.02)
$260 < \sigma_v \leqslant 290\,\mathrm{km\,s^{-1}}$	6195	-0.26	(0.33)	-0.15	(0.58)	0.20	(0.45)
$290 < \sigma_v \leqslant 320\,\mathrm{km\,s^{-1}}$	4835	-0.17	(0.57)	0.05	(0.85)	0.24	(0.41)
$320 < \sigma_v \leqslant 350\,\mathrm{km\,s^{-1}}$	2350	-0.55	(0.16)	-0.02	(0.96)	0.36	(0.39)

these objects and their mass, the more massive the objects the higher their [Z/H] and [α/Fe] .

In Figures 6-7 we have employed HγF, Mg b and $\langle$Fe$\rangle$ when estimating the SSP parameters. In Figure 8 we show the results of using Hβ instead of HγF when re-constructing the age-redshift relationship. The [Z/H] and

[α/Fe] redshift relationships (not shown) are similar to those in Figure 6, but shifted to lower values by approximately 0.05 dex in [Z/H] and 0.01 dex in [α/Fe] . The scatter in Hβ translates into significant scatter in the age estimates but the same trend seen in Figure 6 still exists, i.e. the age of
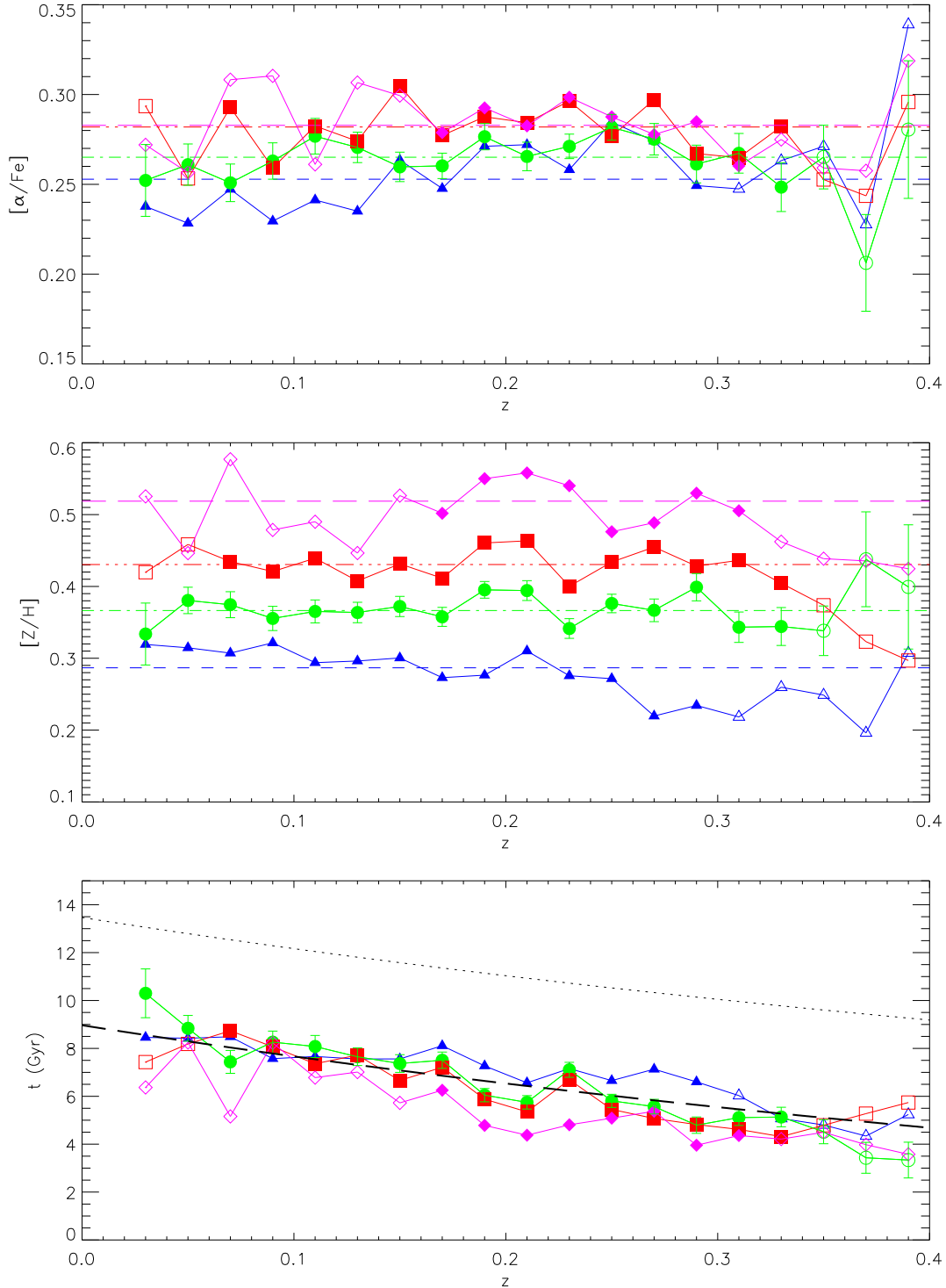
Figure 6. Reconstruction the evolution of the mean luminosity-weighted age, [Z/H] and [α/Fe] using HγF, Mg b , Fe5270 and Fe5335. Symbols and colours are the same as shown in Figure 5. Open symbols represent data with S/N< 100 Å $^{-1}$ in HγF. Horizontal lines represent the mean [Z/H] and [α/Fe] for data with S/N> 100 Å $^{-1}$ in the $230 < \sigma_v \leqslant 260 \,\mathrm{km\,s^{-1}}$ (blue short dash), $260 < \sigma_v \leqslant 290 \,\mathrm{km\,s^{-1}}$ (green dot-dash), $290 < \sigma_v \leqslant 320 \,\mathrm{km\,s^{-1}}$ (red dotted-dash) and $320 < \sigma_v \leqslant 350 \,\mathrm{km\,s^{-1}}$ (pink long dash) samples. For the reconstruction of the age-redshift relationship the dotted line shows the age of the universe $t_U(z)$ for a ΛCDM cosmology while the dashed line indicates $t_U(z) - 4.5 \,\mathrm{Gyr}$ and is for reference only. To reduce clutter in the diagram we again only show the 1σ errors on the $260 < \sigma_v \leqslant 290 \,\mathrm{km\,s^{-1}}$ (circles/green) sample only, but errors for each sample are consistent with the scatter.
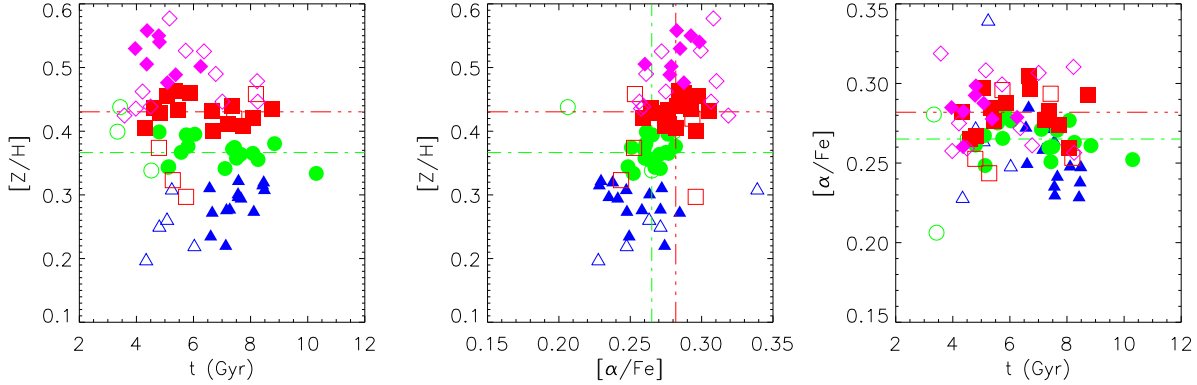
Figure 7. Correlations between the SSP parameters of Figure 6. Parameter estimates are formed from the one-dimensional posterior distribution marginalised over the remaining parameters.

Figure 8. Reconstruction the evolution of the mean luminosity-weighted age using Hβ, Mg b , Fe5270 and Fe5335. The only difference between this figure and Figure 6 is the choice of Balmer line used in the estimation of the SSP parameters. While the trend of the age-redshift relationship is the same as that derived using HγF, there is more variability in the *age* estimates resulting from the variability in Hβ as seen in Figure 5. Also the ages derived using Hβ are systematically older than those derived using HγF. Symbols and lines are the same as in Figure 6 and we have excluded the [Z/H] and [α/Fe] traces here as they are similar to the corresponding traces in Figure 6.

the objects decreases with redshift, although the ages are older by approximately 2.5 Gyr.

4.3   SSP Parameter Estimates - Gaussian Priors

By binning our samples into redshift intervals, we have obtained multiple independent estimates of the chemistry of our LRG population. For each mass sample we can use these independent estimates of [Z/H] and [α/Fe] to produce a prior probability distribution, which we can then employ to better constrain the *age* estimates when estimating the posterior probability using Equation 1. When determining the priors on [Z/H] and [α/Fe], we only use individual estimates that have been produced using line-strength data with S/N> 100 Å^{-1} in HγF and we generate Gaussian priors from the mean and standard error ($rms/\sqrt{n}$) of the [Z/H] and [α/Fe] distributions for a given mass sample. We use *importance sampling* (Lewis & Bridle 2002) and the new

Gaussian priors to re-weight the original MCMC chain data obtained with uniform priors on the parameters. Although [α/Fe] does not correlate with *age*, [Z/H] does (see Figure 3 of TMBO) and placing a prior constraint on [Z/H] results in a tightening of the multivariate posterior distribution yielding a more localised marginalised distribution for the *age* of the object.

In Figure 9 we show what effect the Gaussian priors on [Z/H] and [α/Fe] have on the reconstruction of the *age-redshift* relationship for each mass sample. The impact of the prior on [α/Fe] is negligible, but the decrease in the errors on the individual *age* estimates, and the reduction in the scatter for a given mass sample resulting from the prior on [Z/H], and the age-metallicity degeneracy, is significant. Over the redshift range studied herein, we see a decrease in the age of LRGs of $\simeq$ 5Gyrs, which is fully consistent with expectations from a ΛCDM universe.
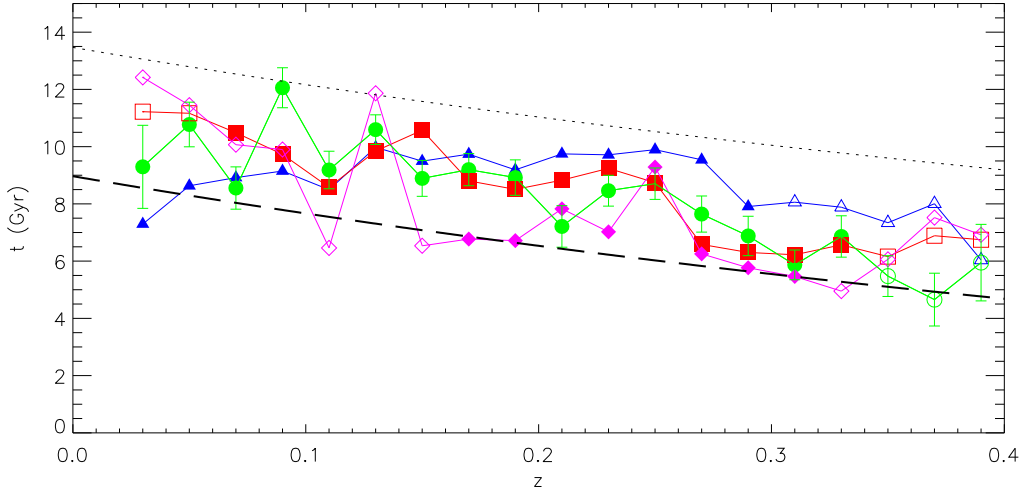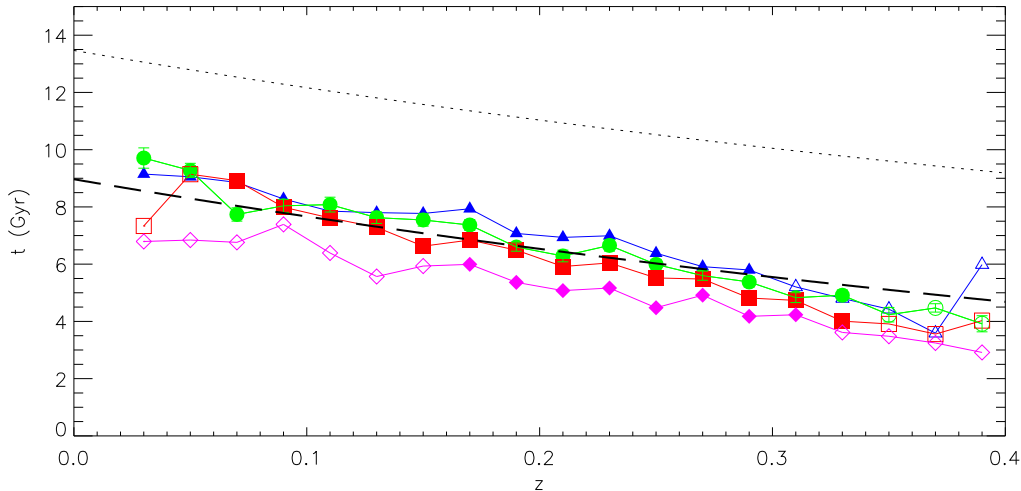
Figure 9. Reconstruction the evolution of the mean luminosity-weighted age using $H\gamma F$, $Mg\,b$, Fe5270 and Fe5335 and employing Gaussian priors on [Z/H] and [α/Fe] . The size of the error bars on the $260 < \sigma_v \leqslant 290\,\mathrm{km\,s^{-1}}$ (circles/green) sample are about the same size as the data points.

5 DISCUSSION

We present in Figures 4, 5, 7, 8 and 9, the results of our analysis of LRG ages, metallicities and α-enhancements as a function of redshift. We also provide in Appendices C and D the data presented in these figures. Overall, these trends are consistent with expectations and can provide important constraints on cosmology (via the age-redshift relation) and galaxy evolution studies. However, we raise here a number of important caveats that should be considered when using these data.

First, we have tried to select a consistent population of quiescent galaxies with redshift using the SDSS Luminous Red Galaxy (LRG) selection, which is designed to select "red and dead" massive galaxies out to $z \sim 0.4$ (with a constant number density). The size of this LRG sample also allows us to preferentially select quiescent galaxies with no obvious emission lines, as well as define four subsamples with the same range of velocity dispersions and luminosities. However, we have employed a simple evolutionary correction that maybe too naive at higher redshift and also performed aperture corrections to velocity dispersion measurements for which it has been necessary to assume that corrections derived at low redshift objects can be applied to higher redshift objects. This assumes no evolution in velocity dispersion, or stellar population distributions, and hence no evolution in the mass distribution, over the range $0.0 < z < 0.4$. Both of these assumptions may impact on the samples used in generating the stacked spectrum and could potentially result in different populations at high and low redshift being probed. This could explain the gradients in the [Z/H] and [α/Fe] -redshift relationships even if each population probed is passively evolving.

While some studies into the luminosity function for the red sequence have shown that the most massive systems show little or no evolution over the redshift range probed in this work, (See Bell et al. 2004; Faber et al. 2007), this may not be true for lower mass systems in our sam-

ple. The anticorrelation between [Z/H] and [α/Fe] for the $230 < \sigma_v \leqslant 260$ sample suggests that the low mass systems become less alpha-enhanced and more metal-enriched at late times. This could arise if our galaxy sample includes a fraction of "blue cloud" galaxies whose star formation is switching off and hence moving onto the red sequence since z=0.4. These low mass systems have been forming stars over longer periods of time and have experienced more chemical enrichment than galaxies with similar velocity dispersions whose star formation switched off at earlier times, giving them lower [α/Fe] and higher [Z/H] at low redshift. This low mass sample, while possibly offering insights into the mechanisms behind galaxy evolution, is less useful in its intended role as a cosmological probe due to the possibility of not accurately tracing a passively evolving sample of galaxies.

There are further complications from adopting the Lick/IDS system when estimating the SSP parameters, even though this is a popular and well-known method. For example, matching the SDSS instrumental resolution to that of the IDS instrument, as well as performing each of the aperture, velocity dispersion and zero-point corrections, potentially introduces a source of error into our line-strengths and thus SSP parameter estimations. Also, the KMT05 models are not perfectly matched to the Lick/IDS system and therefore, the accuracy of our SSP parameter estimates could depend on the difference between the calibration of the data to the models. This difference varies for each of the Lick indices, resulting in the absolute value of any SSP parameter being dependent on the particular set of Lick indices chosen. This is illustrated in Figures 6 & 8 by the discrepancy between the absolute ages for our quiescent LRGs when derived using $H\gamma$ or $H\beta$. Therefore, we would caution the reader from using our absolute ages in this paper, but recommend they focus on the relative ages with redshift.

We also note that our observed line-strengths are strongly dependent on the accuracy of the velocity dispersion correction (see Appendix A). Since the velocity dispersion correction depends on the stellar sample used to gener-

ate the correction factors, matching the stellar sample to the dominant stellar population of the LRG may become important in the future. Also, at higher redshift, the contribution of younger stellar populations to the galaxy spectrum may require a different stellar sample to be used in making the velocity dispersion correction. Therefore, questions remain over the appropriateness of employing a single stellar sample of KIII stars to determine the velocity dispersion correction over the redshift range used in this work.

However, we finish by stressing that for our samples we see little evolution in the shape of [Z/H] and [α/Fe] with redshift, especially for the intermediate mass (velocity dispersion) samples which are consistent with a constant over the redshifts probed. This is re-assuring as it does indicate that our attempts to select a passively evolved, quiescent subsample of galaxies that could be used to probe the age–redshift relation can be found and the errors well-controlled. We provide these relationships here for others to use in their analyses, and plan to explore the cosmological constraints of our *age-redshift* relationships in a subsequent paper.

6   SUMMARY

We present here a detailed analysis of a sample of passive SDSS LRGs which are selected to be the same population of galaxies over the redshift range $0.0 < z < 0.4$. A total of 17,853 LRGs are co-added in four bins of velocity dispersion and luminosity to provide high signal–to-noise spectra for detailed spectra absorption line measurements. In Section 3 and Appendix A, we outline the careful calibration of these absorption line measurements onto the well–established Lick/IDS system which has been extensively used in the literature to constrain Simple Stellar Population (SSP) models and thus derive galaxy parameters like age, metallicity and α–enhancements. In Figures 4, 5, 7 and 8, we present our results which show clear trends for these parameters with redshift (we also provide the data from these figures in Appendices C & D). In particular, for our two intermediate mass (velocity dispersion) samples, we see a constant [Z/H] and [α/Fe] with redshift which confirms our assumptions that these LRGs are a passively evolving subsample of galaxies (i.e., they are chemically unevolved over this redshift range) providing confidence on our age determinations for these galaxies. We see a clear trend of decreasing age of our LRGs as a function of redshift ($\simeq$ 5Gyrs over the redshift range probed here), which is fully consistent with expectations from a ΛCDM universe. It also appears that the most massive sample of LRGs is also the youngest (Figures 5 and 8). We provide these relationships now to help others studying cosmology and galaxy evolution, as well as provide in our appendices, the methodology required for others to calibrate SDSS spectra onto the Lick/IDS system.

REFERENCES

Abazajian K., et al., 2003, AJ, 126, 2081
Adelman-McCarthy J. K., et al., 2006, ApJS, 162, 38
Bell, E. F., et al., 2004, ApJ, 608, 752
Bender R., Burstein D., Faber S. M., 1993, ApJ, 411, 153
Bernardi M., et al., 2003a, AJ, 125, 1817
Bernardi M., et al., 2003b, AJ, 125, 1882
Bernardi M., Nichol R. C., Sheth R. K., Miller C. J., Brinkmann J., 2006, AJ, 131, 1288
Blanton M. R., Roweis S., 2007, AJ, 133, 734
Bruzual G., Charlot S., 2003, MNRAS, 344, 1000
Burstein D., Faber S. M., Gaskell C. M., Krumm N., 1984, ApJ, 287, 586
Cardiel N., 2007, in Figueras F., Girart J. M., Hernanz M., Jordi C., eds, Proceedings of the 7th Scientific Meeting of the Spanish Astronomical Society
Collins, C. A., & Mann, R. G. 1998, MNRAS, 297, 128
Cowan G., 1998, Statistical Data Analysis.. Oxford University Press
de la Rosa I. G., de Carvalho R. R., Vazdekis A., Barbuy B., 2007, AJ, 133, 330
Doran M., Müller C. M., 2004, JCAP, 9, 3
Eisenstein D. J., et al., 2001, AJ, 122, 2267
Eisenstein, D. J., et al. 2003, ApJ, 585, 694
Faber S. M., Friel E. D., Burstein D., Gaskell C. M., 1985, ApJS, 57, 711
Faber S. M., et al., 2007, ApJ, 665, 265
Fukugita M., Nakamura O., Turner E. L., Helmboldt J., Nichol R. C., 2004, ApJL, 601, L127

Gelman A., Rubin D. B., 1992, Statist. Sci., 7, 457

Goudfrooij P., Emsellem E., 1996, A&A, 306, L45

Hastings W. K., 1970, Biometrika, 57, 97

Hog E., Kuzmin A., Bastian U., Fabricius C., Kuimov K., Lindegren L., Makarov V. V., Roeser S., 1998, A&A, 335, L65

Hogg D. W., Finkbeiner D. P., Schlegel D. J., Gunn J. E., 2001, AJ, 122, 2129

Jimenez, R., Verde, L., Treu, T., & Stern, D. 2003, ApJ, 593, 622

Jørgensen I., Franx M., Kjaergaard P., 1995, MNRAS, 276, 1341

Korn A. J., Maraston C., Thomas D., 2005, A&A, 438, 685

Kuntschner H., Lucey J. R., Smith R. J., Hudson M. J., Davies R. L., 2001, MNRAS, 323, 615

Lee Y. S., Beers T. C., Sivarani T., Allende Prieto C., Koesterke L., Wilhelm R., Norris J. E., Bailer-Jones C. A. L., Re Fiorentin P., Rockosi C. M., Yanny B., Newberg H., Covey K. R., 2007, astroph/0710.5645

Lewis A., Bridle S., 2002, PhRvD, 66, 103511

Loubser S. I., Sánchez-Blázquez P., Sansom A. E., Soechting I. K., 2009, MNRAS, 398, 133

Lupton R., Gunn J. E., Ivezić Z., Knapp G. R., Kent S., 2001, in Harnden Jr. F. R., Primini F. A., Payne H. E., eds, Astronomical Data Analysis Software and Systems X Vol. 238 of Astronomical Society of the Pacific Conference Series, The SDSS Imaging Pipelines. p. 269

Maraston C., 1998, MNRAS, 300, 872

Maraston, C., Strömbäck, G., Thomas, D., Wake, D. A., & Nichol, R. C. 2009, MNRAS, 394, L107

McNamara B. J., Sanders W. L., 1978, A&A, 62, 259

McNamara B. J., Solomon S., 1981, A&AS, 43, 337

Mehlert D., Saglia R. P., Bender R., Wegner G., 2000, A&AS, 141, 449

Mehlert D., Thomas D., Saglia R. P., Bender R., Wegner G., 2003, A&A, 407, 423

Metropolis N., Rosenbluth A. W., Rosenbluth M. N., Teller A. H., Teller E., 1953, J. Chem. Phys., 21, 1087

Moore S. A. W., Lucey J. R., Kuntschner H., Colless M., 2002, MNRAS, 336, 382

Morton D. C., 1991, ApJS, 77, 119

Pier J. R., Munn J. A., Hindsley R. B., Hennessy G. S., Kent S. M., Lupton R. H., Ivezić Ž., 2003, AJ, 125, 1559

Poggianti B. M., Bridges T. J., Carter D., Mobasher B., Doi M., Iye M., Kashikawa N., Komiyama Y., Okamura S., Sekiguchi M., Shimasaku K., Yagi M., Yasuda N., 2001, ApJ, 563, 118

Robinson L. B., Wampler E. J., 1972, PASP, 84, 161

Roseboom I. G., et al., 2006, MNRAS, 373, 349

Simon, J., Verde, L., & Jimenez, R. 2005, PhRvD, 71, 123001

Stern, D., Jimenez, R., Verde, L., Kamionkowski, M., & Stanford, S. A. 2009, arXiv:0907.3149

Stoughton C., et al., 2002, AJ, 123, 485

Strauss M. A., et al., 2002, AJ, 124, 1810

Thomas D., Maraston C., Bender R., 2003, MNRAS, 339, 897

Thomas D., Maraston C., Bender R., Mendes de Oliveira C., 2005, ApJ, 621, 673

Trager S. C., Worthey G., Faber S. M., Burstein D., González J. J., 1998, ApJS, 116, 1

Tremonti C. A., et al., 2004, ApJ, 613, 898

Verde L., et al., 2003, ApJS, 148, 195

Wake D. A., et al., 2006, MNRAS, 372, 537

Worthey G., Faber S. M., González J. J., Burstein D., 1994, ApJS, 94, 687

Worthey G., Ottaviani D. L., 1997, ApJS, 111, 377

Worthey G., 1998, PASP, 110, 888

Yan R., Newman J. A., Faber S. M., Konidaris N., Koo D., Davis M., 2006, ApJ, 648, 281

York D. G., et al., 2000, AJ, 120, 1579

Zhao Y.-H., Gu Q.-S., Peng Z.-X., Shi L., Luo X.-L., Peng Q.-H., 2006, Chinese Journal of Astronomy and Astrophysics

APPENDIX A: CALIBRATING TO LICK/IDS SYSTEM

We provide here the details of our calibration of SDSS spectra onto the Lick/IDS system. We use the most recent definitions of the Lick indices from Trager et al. (1998) and Worthey & Ottaviani (1997), while the index line-strengths are calculated using the standard equations

$$I_a\,(\text{Å}) \equiv \int_{\lambda_{c_1}}^{\lambda_{c_2}} \left[1 - \frac{F(\lambda)}{C(\lambda)}\right] d\lambda\,, \tag{A1}$$

and

$$I_m\,(\text{mag}) \equiv -2.5 \log_{10}\left\{\frac{\int_{\lambda_{c_1}}^{\lambda_{c_2}} [F(\lambda)/C(\lambda)]\,d\lambda}{\lambda_{c_2} - \lambda_{c_1}}\right\}, \tag{A2}$$

where the narrow feature atomic indices, I_a, have their line-strengths expressed in Angstroms (Å) while the broad feature molecular indices, I_m, are expressed in magnitudes (mag). Also, in Equations A1 and A2, λ_{c_1} and λ_{c_2} are the wavelength definitions of the feature bandpass and $F(\lambda)$ and $C(\lambda)$ are the flux in the index bandpass and pseudocontinuum respectively. When measuring the line-strengths of absorption features we use the software package INDEXF (Cardiel 2007).

The flux in the local pseudocontinuum, $C(\lambda)$, is determined using

$$C(\lambda) \equiv F_b \frac{\lambda_r - \lambda}{\lambda_r - \lambda_b} + F_r \frac{\lambda - \lambda_b}{\lambda_r - \lambda_b}\,, \tag{A3}$$

where

$$F_b \equiv \int_{\lambda_{b_1}}^{\lambda_{b_2}} \frac{F(\lambda)}{\lambda_{b_2} - \lambda_{b_1}}\,d\lambda\,, \tag{A4}$$

and

$$F_r \equiv \int_{\lambda_{r_1}}^{\lambda_{r_2}} \frac{F(\lambda)}{\lambda_{r_2} - \lambda_{r_1}}\,d\lambda\,, \tag{A5}$$

and

$$\lambda_b \equiv (\lambda_{b_2} + \lambda_{b_1})/2\,, \quad \lambda_r \equiv (\lambda_{r_2} + \lambda_{r_1})/2\,. \tag{A6}$$

λ_{b_1}, λ_{b_2}, λ_{r_1} and λ_{r_2} are the wavelength definitions of the blue and red bandpasses. The resulting local pseudocontinuum, $C(\lambda)$, generated by this approach is a straight line that connects the average flux, defined at the central wavelength, of the blue (F_b, λ_b) and red (F_r, λ_r) bandpasses of the index.

A1   Transforming to Lick/IDS

Since the Lick indices have been defined with spectra taken on the IDS, the absorption index system developed by the Lick group has the characteristics of the IDS instrument inherent to it. Also, the spectra obtained by the Lick group were not flux calibrated and this results in the shape of the continuum of a Lick/IDS spectra differing to the true shape. Line-strengths measured on spectra not observed with the IDS instrument need to be transformed to the Lick/IDS system such that they can be compared with Lick/IDS calibrated SSP models. For galaxy spectra this requires that spectra are smoothed to the IDS resolution and line-strengths are corrected for aperture and velocity dispersion effects and zero-point corrections applied. These steps are described in more detail in the following subsections.

A2   Matching Instrumental Resolutions

The measured line-strength of a given Lick Index depends on, amongst other things, the instrumental resolution. As a result of the fixed wavelength definitions of the index bandpasses and pseudocontinua, the line-strength generally decreases as the instrumental resolution is degraded. This instrumental broadening causes the wings of the spectral feature to extend outside their bandpass window reducing the strength of the absorption feature within the window. In addition to this, adjacent spectral features may depress the flux in the continuum by being broadened into the continuum windows reducing the line-strength further.

In order to transform SDSS spectra to the Lick/IDS system, it is necessary to degrade the higher resolution SDSS spectra to match the lower resolution of the IDS instrument. But, because the Lick/IDS calibrated SSP models produce index strengths for a stellar population in the rest frame at the resolution of the Lick/IDS system, it is necessary to ensure that the absorption feature in the observed spectrum has the same instrumental resolution as it would have at rest in the Lick/IDS system.

The SDSS spectrographs have 640 fibers with the spectral resolution of each fiber having a slightly different dependence with wavelength. The response of the IDS instrument can be treated as a Gaussian of wavelength dependent width (Worthey & Ottaviani 1997) and to match instrumental resolutions, the SDSS spectra were convolved with a Gaussian whose wavelength dependent width was found using

$$\sigma_{\rm Lick}^2((1+z)\,\lambda_{\rm Lick}) = \sigma_{\rm SDSS}^2(\lambda_{\rm obs}) + \sigma_{\rm match}^2\,(\lambda_{\rm obs})\,, \quad \text{(A7)}$$

where $\sigma_{\rm match}(\lambda_{\rm obs})$ is the width of the Gaussian required to match the Lick/IDS and SDSS spectral resolutions, $\sigma_{\rm Lick}((1+z)\,\lambda_{\rm Lick})$ is the wavelength dependent spectral resolution of the Lick/IDS instrument shifted to the observed frame and $\sigma_{\rm SDSS}(\lambda_{\rm observed})$ is the SDSS resolution for a particular fiber.

The SDSS spectral resolution is determined for each object separately using information in the header (HDU #6) of the FITS file for a given object. This header contains the RMS resolution (in pixels) as a function of pixel number and to convert from RMS resolution in pixel units to RMS resolution in wavelength units, the RMS resolution in pixels is multiplied by the local pixel size in wavelength units

$$\sigma_\lambda = \sigma_{\rm pix} \times \ln(10) \times \lambda_{\rm pix} \times 10^{-4}\,, \quad \text{(A8)}$$

where $\lambda_{\rm pix}$ is the wavelength at a given pixel and the factor 10^{-4} is a result of the SDSS spectra being binned with constant logarithmic dispersion of this size.

The convolution of the SDSS spectra with a Gaussian was performed in pixel space and is given by

$$(S \otimes G(j))_j = \sum_{i=0}^{m-1} S_{j+i-m/2}\, G_i(j)\,, \quad \text{(A9)}$$

where S is the science spectrum, $G(j)$ is the variable width Gaussian and m is the width of the Gaussian window function and is set at 4.5 times the FWHM of the Gaussian. The width of the Gaussian is wavelength dependent, which in pixel space means that the width is a function of pixel location j. At each pixel j, a normalized Gaussian is generated whose width in pixels is determined from Equations A7 and A8, where $\sigma_{\rm Lick}(\lambda)$ is inferred from linear interpolation of the data in Table 8 of Worthey & Ottaviani (1997), after converting the air wavelengths in the table to vacuum wavelengths and redshifting to the frame of the observed spectrum, $\lambda_{\rm obs} = (1+z)\,\lambda_{\rm Lick}$.

As a result of this convolution procedure, the resolution of the SDSS spectra at the observed wavelength is matched to the resolution at the corresponding rest-frame wavelength on the Lick/IDS system, and consequently absorption features measured in the target spectrum match the resolution of the same feature on the Lick/IDS system.

A3   Velocity Dispersion Corrections

The observed spectrum of a galaxy is equivalent to the convolution of the instrumental response function, the distribution of the line-of-sight velocities of its stars and their integrated spectrum. The velocity dispersion of the galaxy and the instrumental response both broaden spectral features, thereby depressing the measured line-strengths from their intrinsic value.

The Lick/IDS system is based upon an empirical stellar library and is therefore defined at zero intrinsic velocity dispersion. In order to compare galaxy index measurements to their SSP model predictions, the raw measurements need to be corrected to zero velocity dispersion.

To generate the correction factors, we adopted the approach of Poggianti et al. (2001), which involves matching the resolution of a sample of SDSS stellar spectra to the Lick/IDS resolution. Then, each stellar spectrum was further convolved with a Gaussian, in logarithmic wavelength space, to mimic the velocity dispersion of a galaxy and was repeated for velocity dispersions in the range $\sigma = 0 - 420\,{\rm km\,s^{-1}}$ in steps of $20\,{\rm km\,s^{-1}}$.

When estimating velocity dispersions, the SDSS pipeline uses template spectra which are convolved to a maximum velocity dispersion of $420\,{\rm km s^{-1}}$, which we then adopt as the maximum velocity dispersion to broaden our stellar spectra by. Incidentally, the template spectra used by the SDSS pipeline are stellar spectra taken from plate 321, the same plate used in this work to calibrate the systematic offsets and place the SDSS on the Lick/IDS system.

The selection of the stellar spectra used to generate the correction factors utilises the SEGUE Stellar Parameter Pipeline (SSPP; Lee et al. 2007) database via the CAS. As part of the SSPP, the stellar spectra are cross-correlated

Table A1. Polynomial fits to the velocity dispersion correction factors

Index	b_0	b_1 $(\times 10^{-3})$	b_2 $(\times 10^{-6})$	b_3 $(\times 10^{-9})$
CN1	0.000	0.002	0.077	-0.071
CN2	-0.000	0.002	0.226	-0.222
Ca4227	0.991	0.420	0.259	11.978
G4300	0.999	0.034	0.390	0.220
Fe4383	0.998	0.035	2.035	-0.803
Ca4455	0.986	0.249	2.919	3.582
Fe4531	0.998	0.039	1.401	0.526
C4668	1.000	-0.013	1.148	-0.037
Hbeta	1.003	0.037	-0.256	1.105
Fe5015	0.999	0.075	2.682	-1.948
Mg1	0.000	-0.001	0.076	-0.091
Mg2	-0.000	0.004	0.020	0.029
Mgb5177	1.001	-0.041	2.338	-0.555
Fe5270	1.001	0.064	2.687	-1.730
Fe5335	1.004	0.033	4.967	0.823
Fe5406	1.004	-0.074	5.100	1.181
Fe5709	0.995	0.146	0.905	3.824
Fe5782	0.999	0.105	3.533	4.859
Na5895	1.002	0.051	0.259	2.013
TiO1	-0.000	-0.001	0.023	-0.021
TiO2	-0.000	-0.000	0.016	-0.013
HdA	0.999	0.013	0.996	-0.421
HgA	1.000	-0.013	-0.081	0.918
HdF	0.991	0.054	-1.457	1.398
HgF	1.001	0.019	0.958	-1.437

Table A2. Lick index zero-point offsets

Index	mean $\pm$ rms	N	significance
CN_1	0.013 ± 0.023	13	2.0σ
CN_2	0.008 ± 0.022	13	1.4σ
Ca4227	0.095 ± 0.330	13	1.0σ
G4300	0.037 ± 0.384	13	0.3σ
Fe4383	-0.556 ± 0.890	13	2.3σ
Ca4455	-0.374 ± 0.440	13	3.1σ
Fe4531	0.083 ± 0.404	13	0.7σ
C_24668	-0.001 ± 0.626	12	0.0σ
$H\beta$	0.105 ± 0.285	13	1.3σ
Fe5015	-0.340 ± 0.581	12	2.0σ
Mg_1	-0.018 ± 0.021	12	3.1σ
Mg_2	-0.028 ± 0.030	12	3.2σ
Mg_b	0.181 ± 0.318	12	2.0σ
Fe5270	0.011 ± 0.252	13	0.2σ
Fe5335	0.057 ± 0.227	13	0.9σ
Fe5406	0.011 ± 0.181	13	0.2σ
Fe5709	-0.099 ± 0.167	13	2.1σ
Fe5782	-0.104 ± 0.189	12	1.9σ
Na D	-0.650 ± 0.724	13	3.2σ
TiO_1	-0.006 ± 0.009	12	2.1σ
TiO_2	0.005 ± 0.010	11	1.8σ
$H\delta_A$	0.341 ± 0.804	12	1.5σ
$H\gamma_A$	-0.499 ± 0.836	13	2.2σ
$H\delta_F$	0.183 ± 0.421	12	1.5σ
$H\gamma_F$	-0.107 ± 0.269	13	1.4σ

with ELODIE () high resolution spectra, degraded to match the SDSS resolution, to determine radial velocities. Those spectra whose best matching template was a K0-K3 III star were used to create a sample from which the velocity dispersion correction factors were produced.

The index strengths for each star at each broadened velocity dispersion were measured and compared to the index strength from the zero-velocity dispersion stellar spectra. The correction factors $C_I(\sigma) = \text{Index}(\sigma = 0)/\text{Index}(\sigma)$ for atomic indices, and $C_I(\sigma) = \text{Index}(\sigma = 0) - \text{Index}(\sigma)$ for molecular indices, were generated from the broadened spectra.

We then fit a polynomial of the form

$$C_I(\sigma) = \sum_{0 \leqslant i \leqslant 3} b_i \sigma^i, \tag{A10}$$

to the correction factor data for each index where σ represents the velocity dispersion. This polynomial fit is employed when making velocity dispersion corrections to a given line-strength. In Figure A1 we show the correction factors and the best fitting polynomial for each index. In Table A1 we present the coefficients of the best fitting polynomial to C_I for each Lick index.

A4 Zero-Point Corrections

The Lick/IDS spectra were not flux calibrated but instead normalized to a calibration lamp. Differences between the continuum of the fluxed SDSS spectra and normalized Lick/IDS spectra will manifest themselves as systematic offsets between our measured line strengths and those of common objects already on the Lick/IDS system. To determine

these offsets, and hence facilitate the use of SSP models calibrated to the Lick/IDS system, it is necessary to measure the line strengths of Lick stars that are common to SDSS.

Using spectra of the 11 stars in M67 and 2 stars in NGC 7789 previously identified as Lick stars, we have matched resolutions to the Lick/IDS and measured line-strengths for all 25 Lick indices. In Figure A2 we show the comparison between our measurements and those of Worthey et al. (1994) for the 13 Lick stars observed by SDSS. In Table A2 the statistical significance of the mean offset ($|offset|/\sigma$) for the majority of indices can be seen to be less than 2σ, where $\sigma = rms/\sqrt{N}$. Consequently, we choose only to apply zero-point offsets to those indices with offsets that have $> 2\sigma$ significance and these are shown in Figure A2 as panels with bold borders.

A5 Aperture Corrections

The measured velocity dispersion and the line-strengths of absorption features for a galaxy is affected by a number of factors which include the size and shape of the spectrograph aperture used to sample the light from the galaxy, the distance to the galaxy, the luminosity distribution and the distribution of stellar velocities.

Elliptical galaxies exhibit radial gradients in their velocity dispersions as well as in their absorption-line indices (Mehlert et al. 2000), and it is necessary to correct for these gradients when comparing our results to other results in the literature. Corrections are also necessary when comparing data over a large range in redshift as the fixed spectrograph aperture will sample different physical scales depending on the distance to the galaxy.

A further complication when comparing results to those
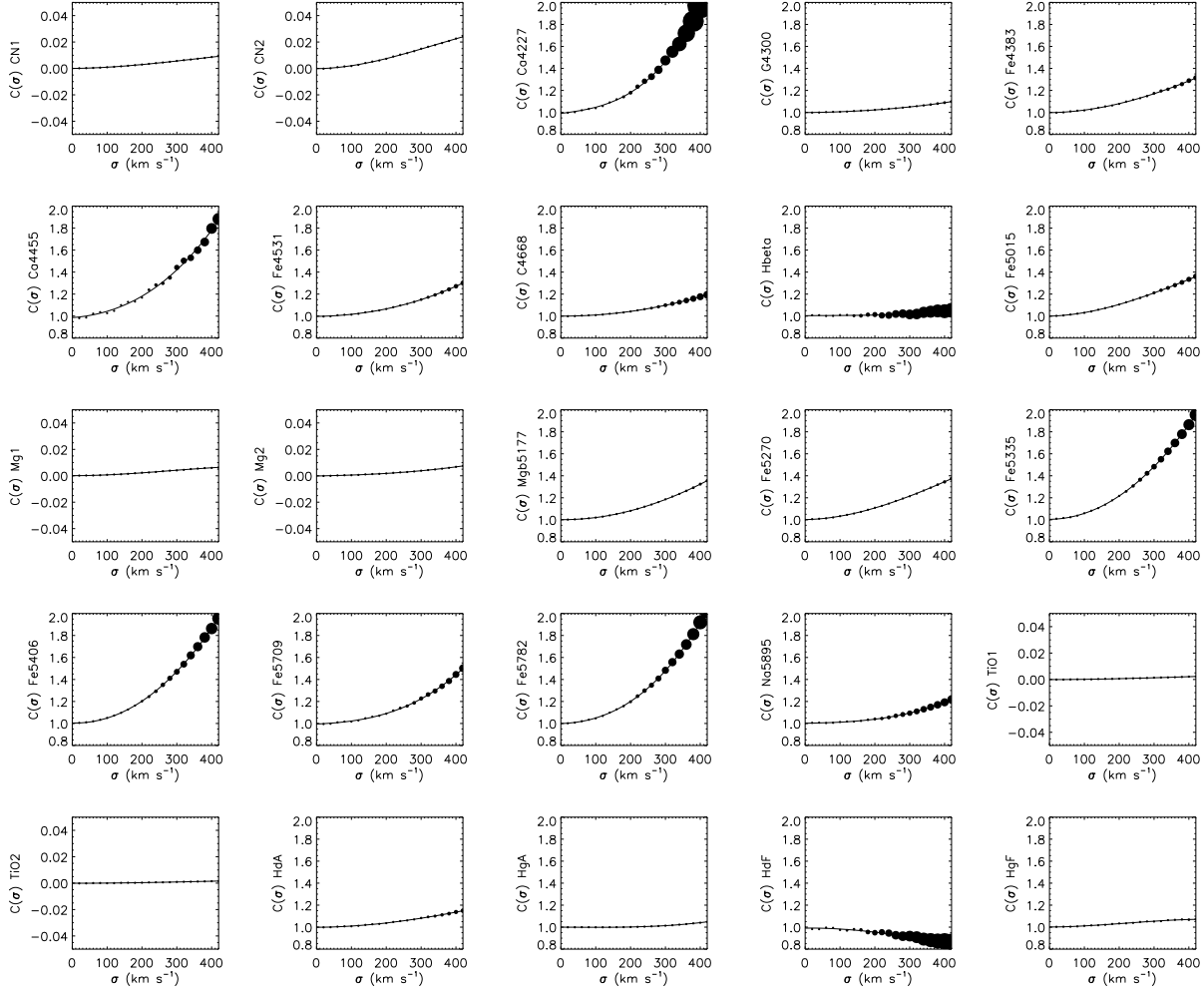
Figure A1. Velocity dispersion correction curves for each Lick index, determined from a sample of 31 K III stars. The size of the symbol at a given σ indicates the magnitude of the standard deviation in correction factors for the stellar sample used.

in the literature is the size and shape of the spectrograph aperture used. We use the method of Jørgensen et al. (1995) to convert rectangular apertures to an equivalent circular aperture of radius r_{ap}. They show that a velocity dispersion estimated with a circular aperture would yield the same mean value, to within 4%, as that through a rectangular aperture if $2r_{ap} = 1.025 \times 2(xy/\pi)^{1/2}$, where x and y are the dimensions of the rectangular aperture.

Jørgensen et al. also show how the velocity dispersion, measured with a circular aperture, varies with aperture radius and they have determined that within an effective radius, the velocity dispersion profile normalised to σ_{e8}, can be approximated by a power law of the form

$$\frac{\sigma_{ap}}{\sigma_{e8}} = \left(\frac{r_{ap}}{r_e/8}\right)^{\alpha} , \tag{A11}$$

where α is the gradient in the velocity dispersion, r_e is the effective radius of the galaxy and σ_{e8} is the velocity dispersion measured through an aperture of $r_e/8$.

Using Equation A11, and following the approach of Bernardi et al. (2003a), we correct the measured velocity dispersion, σ_{ap}, returned by the SDSS pipeline to a veloc-

ity dispersion, $\sigma_{corr} \equiv \sigma_{e8}$, that would be measured through $r_e/8$. From $r_e \equiv (b/a)^{1/2} r_{deV}$, we determined r_e, where r_{deV} is the de Vaucouleurs radius, b is the semi-minor axis and a is the semi-major axis of the galaxy, i.e. r_e is the effective circular radius. We use the values of r_{deV}, a and b determined from the SDSS r-band photometry and obtained using the parameters `deVrad_r` and `deVAB_r` from the CAS.

Similar expressions to Equation A11 are used to correct the measured line-strengths to the standard-size aperture

$$\log I_{corr} = \log I_{r_{ap}} - \alpha_I \log \frac{r_{ap}}{r_e/8} , \tag{A12}$$

for atomic indices and

$$I_{corr} = I_{r_{ap}} - \alpha_I \log \frac{r_{ap}}{r_e/8} , \tag{A13}$$

for molecular indices, where α_I is the radial gradient $(\Delta \log I/\Delta \log r)$ for the index and $I_{r_{ap}}$ is the line-strength measured from the SDSS spectra.

In order to correct the velocity dispersions and index measurements for aperture effects we adopt the index gradients of Mehlert et al. (2003), in which they have determined gradients for Hβ, Mg b, Fe5270, Fe5335 and the velocity dispersion, σ, for a sample of 35 early-type galaxies.
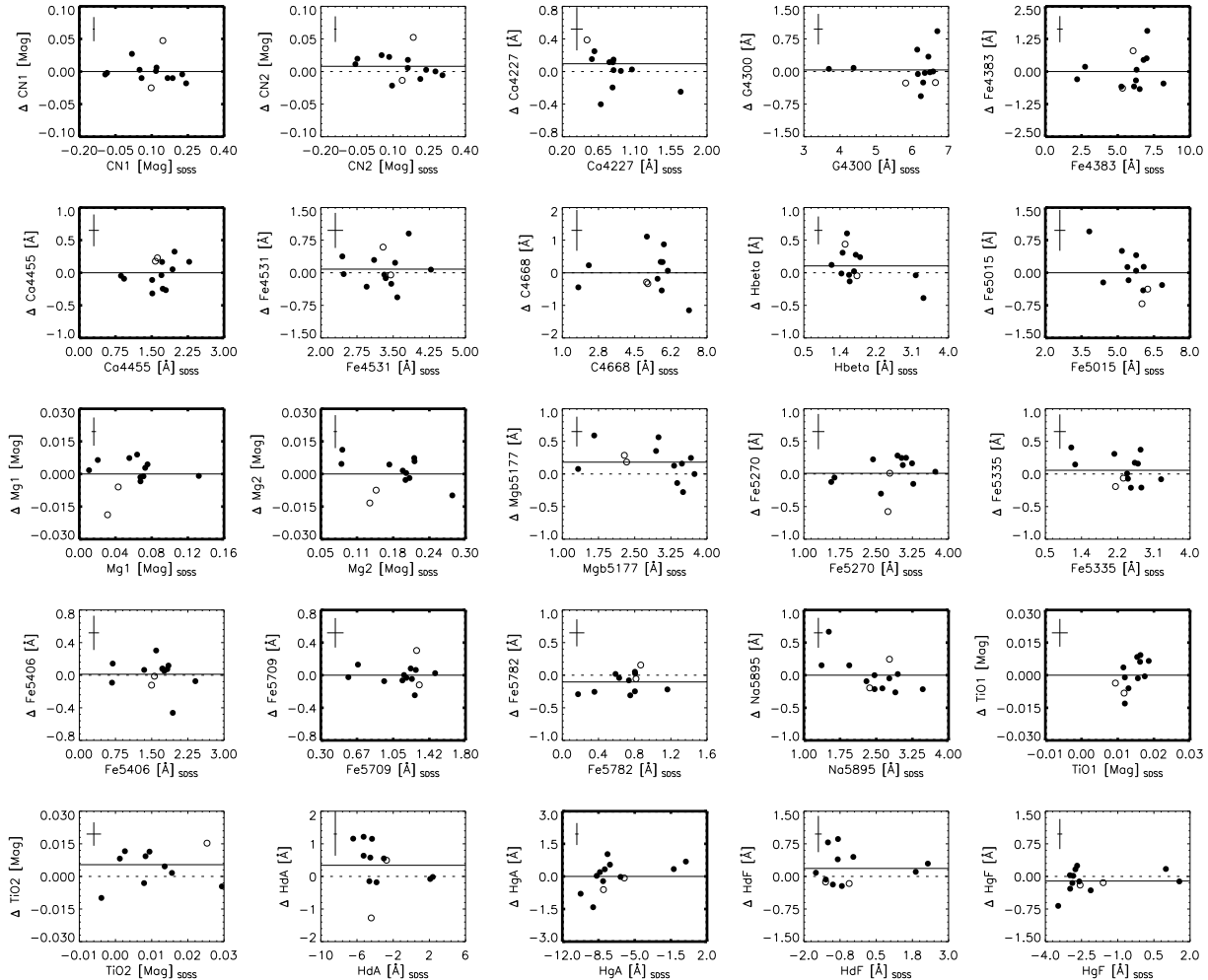
Figure A2. Comparison between our measurements for the 25 indices of Lick/IDS system and those of Worthey et al. (1994), for 11 stars in the open cluster M 67 (closed symbols) and 2 stars on the open cluster NGC 7789 (open symbols) observed by SDSS. The mean offset for each index is indicated by the solid line. Some panels have less that 13 data points because of missing data from either the Worthey et al. dataset or our own. Indices whose systematic offset is determined to be $> 2\sigma$ have had the correction applied and are shown as having bold borders. The median error bar is indicated for each index and Δ Index is in the sense SDSS - Worthey.

A6   Comparison with Previous Data

In order to test our transformation/calibration to the Lick/IDS system it is necessary to perform similar comparisons to that already used in determining the zero-point offsets. There exists extensive work in the literature where authors have obtained line-strengths determined from galaxy spectra and have also calibrated their line-strengths to the Lick/IDS system. Not every source in the literature explores the full set of Lick indices so we restrict our comparison to Hβ , Mg b , Fe5270 and Fe5335. All objects that have been selected for study in this comparison have been matched to within 5" of an SDSS object and have a velocity dispersion available from the SDSS pipeline.

Moore et al. (2002) have observed early-type galaxies in Coma of which 49 have SDSS spectra. All data, both literature and SDSS, have been corrected to a standard circular aperture of $r_e/8$, where r_e has been determined for each object from their SDSS r-band photometric parameters and the method outlined in Section A5. From Figure A3 and Ta-

Table A3. Testing the calibration to Lick/IDS System using Coma galaxies common to SDSS and Moore et al.

Lick Index	Objects with S/N > 30 Å $^{-1}$	All Objects
Hβ	+0.05	+0.06
Mg b	+0.03	−0.06
Fe5270	+0.01	+0.02
Fe5335	+0.02	−0.04

ble A3, it would seem that our calibration to the Lick/IDS system is within approximately 0.05 Å.

Given that the 2.7" fiber used by Moore et al. matches well to the 3" fiber used by SDSS, aperture corrections between these two datasets will be a minimum. The velocity dispersion corrections derived by Moore et al. also match to those derived in this work to better than $\sim 1\%$
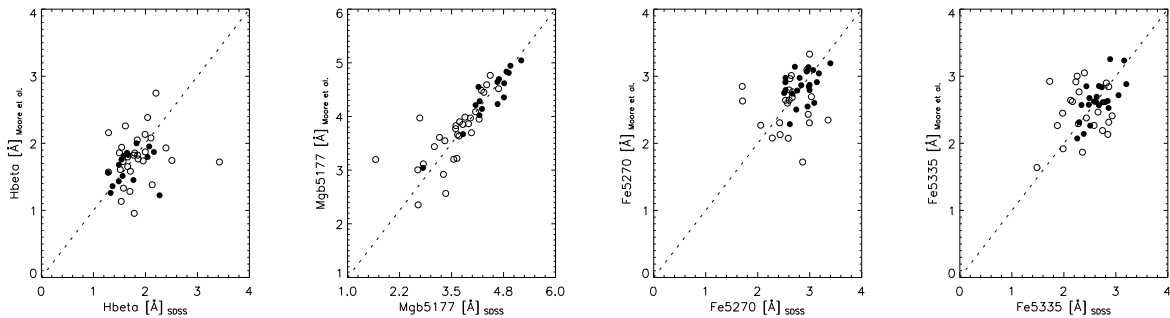
Figure A3. Comparison of line-strengths for Hβ , Mg b , Fe5270 and Fe5335 with Moore et al. (2002) for 49 early-type galaxies in the Coma cluster. All SDSS spectra have been matched to the Lick/IDS resolution, line-strengths corrected (both SDSS and literature measurements) to a standard circular aperture of $r_e/8$ and have been corrected for velocity dispersion effects. For these indices no zero-point corrections have been applied to the SDSS line-strengths as the corrections are not statistically significant, see Section A4. Closed symbols represent indices with SNR > 30 Å^{-1}, while open symbols have SNR less than this value. The dashed line shows the one-to-one correspondence.

at $\sigma \sim 300$ km s^{-1} for the indices that are common between our two studies.

APPENDIX B: TESTING THE MCMC APPROACH TO SSP PARAMETER ESTIMATION

To test our MCMC implementation we have chosen to compare against the Monte Carlo approach of TMBO. We perform a similar test to TMBO, using a model object with an age of 10.7 Gyr, [Z/H] = 0.26 and [α/Fe] = 0.25, which yields line-strengths of Hβ = 1.59 Å, Mg b = 4.73 Å and ⟨Fe⟩ = 2.84 Å. Adopting these line-strengths and the associated errors of d Hβ = 0.06 Å, d Mg b = 0.06 Å and d ⟨Fe⟩ = 0.05 Å we then employ our MCMC approach to recover the original model object SSP parameters and also obtain the errors on the parameters associated with the adopted errors on the line-strengths. When evaluating Equation 1 we employ uniform base priors which cover the full support of each of the SSP parameters and we recover the same bivariate parameter distributions as those shown in Figure 3 of TMBO.

We have also estimated the SSP parameters for 123 early-type galaxies from Table 2 of TMBO and use their line-strength data and our MCMC implementation, where the MCMC simulation for each object consists of 3 parallel chains each of which is 10,000 iterations in size. We use the Gelman-Rubin $\widehat{\mathcal{R}}$-statistic to determine when convergence to the stationary distribution has occurred and exclude the burn-in phase of each chain before pooling the data for the three chains and estimating one-dimensional marginalised posterior parameters. We show the results of this comparison in Figure B1.

The results of this comparison indicates that our MCMC approach is able to produce reliable parameter estimates and errors. In Table B1 our errors are slightly larger than those of TMBO but a similar comparison for the data in Figure B1 would suggest that our errors are generally in good agreement. A more detailed error analysis is prohibited by the fact that we report errors based on the 15.9 and 84.2 percentiles of the marginalised posterior distribution,

Table B1. Comparing MCMC errors to MC errors from TMBO

	model value	TMBO error	MCMC error[a]
age (Gyr)	10.7	±1.48	$+1.57$ [b] -1.48
[Z/H]	0.26	±0.04	$+0.05$ [c] -0.05
[α/Fe]	0.25	±0.02	$+0.05$ [d] -0.05

[a] errors correspond to the central 68.3% of the distributions
[b] base prior, age (Gyr) $\sim \mathcal{U}(0.31, 18.2)$
[c] base prior, [Z/H] $\sim \mathcal{U}(-1.0, 0.97)$
[d] base prior, [α/Fe] $\sim \mathcal{U}(-0.25, 0.73)$

and so can obtain asymmetric errors, while TMBO report symmetric errors.

APPENDIX C: LICK INDEX LINE STRENGTH DATA

We provide here the line-strength data for the Lick indices used in estimating the SSP parameters in Figures 6-9. Line strengths were measured on coadded spectra calibrated to the Lick/IDS system, described in Appendix A, after selecting individual objects using the strategy described in Section 2. In Tables C1-C4 we show line-strengths and their 1σ errors.
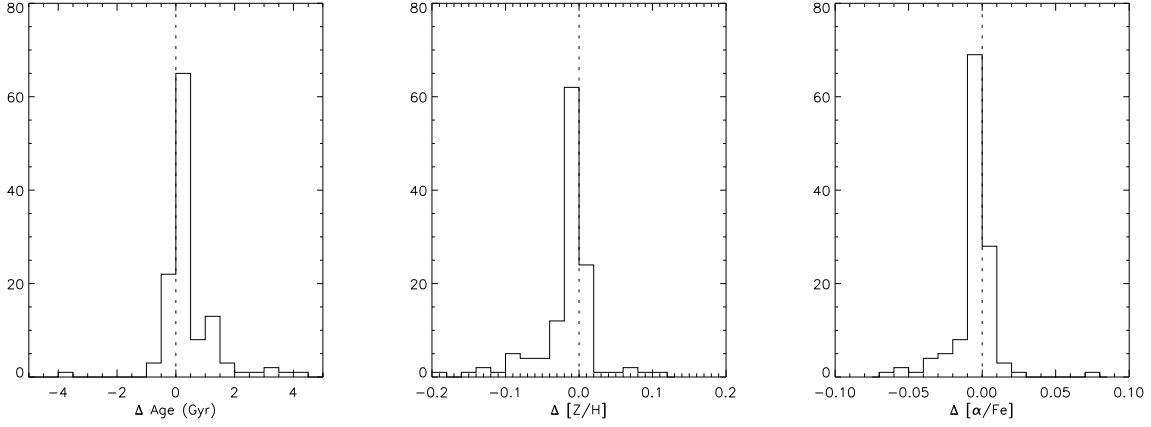
Figure B1. Here we show the residual differences between the MCMC approach of this work and the MC approach of TMBO for 123 early-type galaxies. For a small number of objects our approach yields slightly older ages than TMBO and consequently lower metallicities as a result of the age-metallicity degeneracy, hence the tail of the distributions to older ages and lower metallicities. Differences are in the sense, this work - literature.

Table C1. Fully Calibrated Line Strength Measurements for $230 < \sigma_v \leqslant 260 \mathrm{kms}^{-1}$ mass sample.

Redshift Interval	Hβ (Å)	HγF (Å)	Mg b (Å)	Fe5270 (Å)	Fe5335 (Å)
$0.02 < z \leqslant 0.04$	1.728 ± 0.046	-1.635 ± 0.048	4.688 ± 0.054	2.993 ± 0.063	2.791 ± 0.085
$0.04 < z \leqslant 0.06$	1.671 ± 0.030	-1.632 ± 0.032	4.644 ± 0.035	3.007 ± 0.041	2.786 ± 0.055
$0.06 < z \leqslant 0.08$	1.669 ± 0.022	-1.600 ± 0.023	4.669 ± 0.027	2.956 ± 0.030	2.743 ± 0.039
$0.08 < z \leqslant 0.10$	1.655 ± 0.023	-1.539 ± 0.025	4.598 ± 0.028	3.004 ± 0.032	2.760 ± 0.043
$0.10 < z \leqslant 0.12$	1.698 ± 0.022	-1.488 ± 0.024	4.564 ± 0.030	2.906 ± 0.033	2.742 ± 0.037
$0.12 < z \leqslant 0.14$	1.634 ± 0.021	-1.484 ± 0.022	4.549 ± 0.029	2.917 ± 0.027	2.752 ± 0.031
$0.14 < z \leqslant 0.16$	1.660 ± 0.025	-1.458 ± 0.026	4.621 ± 0.030	2.908 ± 0.029	2.670 ± 0.036
$0.16 < z \leqslant 0.18$	1.651 ± 0.028	-1.496 ± 0.028	4.563 ± 0.029	2.906 ± 0.031	2.677 ± 0.040
$0.18 < z \leqslant 0.20$	1.688 ± 0.031	-1.371 ± 0.030	4.559 ± 0.030	2.843 ± 0.033	2.623 ± 0.040
$0.20 < z \leqslant 0.22$	1.654 ± 0.034	-1.337 ± 0.032	4.587 ± 0.033	2.881 ± 0.033	2.644 ± 0.040
$0.22 < z \leqslant 0.24$	1.664 ± 0.026	-1.369 ± 0.029	4.519 ± 0.028	2.830 ± 0.029	2.677 ± 0.037
$0.24 < z \leqslant 0.26$	1.668 ± 0.028	-1.268 ± 0.034	4.530 ± 0.030	2.843 ± 0.033	2.535 ± 0.039
$0.26 < z \leqslant 0.28$	1.698 ± 0.032	-1.256 ± 0.042	4.422 ± 0.037	2.808 ± 0.036	2.487 ± 0.046
$0.28 < z \leqslant 0.30$	1.760 ± 0.037	-1.236 ± 0.052	4.369 ± 0.040	2.837 ± 0.043	2.567 ± 0.061
$0.30 < z \leqslant 0.32$	1.764 ± 0.036	-1.126 ± 0.058	4.285 ± 0.043	2.793 ± 0.052	2.554 ± 0.062
$0.32 < z \leqslant 0.34$	1.772 ± 0.042	-0.982 ± 0.074	4.310 ± 0.061	2.756 ± 0.061	2.566 ± 0.072
$0.34 < z \leqslant 0.36$	1.812 ± 0.056	-0.878 ± 0.102	4.269 ± 0.074	2.763 ± 0.074	2.478 ± 0.097
$0.36 < z \leqslant 0.38$	1.791 ± 0.073	-0.701 ± 0.129	4.005 ± 0.101	2.768 ± 0.119	2.456 ± 0.185
$0.38 < z \leqslant 0.40$	1.885 ± 0.121	-1.014 ± 0.189	4.684 ± 0.179	2.937 ± 0.259	2.407 ± 0.276

Table C2. Fully Calibrated Line Strength Measurements for $260 < \sigma_v \leqslant 290 \mathrm{kms}^{-1}$ mass sample.

Redshift Interval	Hβ (Å)	HγF (Å)	Mg b (Å)	Fe5270 (Å)	Fe5335 (Å)
$0.02 < z \leqslant 0.04$	1.612 ± 0.052	-1.872 ± 0.054	4.916 ± 0.060	3.117 ± 0.071	2.784 ± 0.098
$0.04 < z \leqslant 0.06$	1.552 ± 0.031	-1.773 ± 0.033	4.934 ± 0.037	3.054 ± 0.042	2.857 ± 0.059
$0.06 < z \leqslant 0.08$	1.659 ± 0.027	-1.603 ± 0.028	4.780 ± 0.033	3.014 ± 0.037	2.842 ± 0.050
$0.08 < z \leqslant 0.10$	1.519 ± 0.025	-1.641 ± 0.027	4.811 ± 0.032	3.014 ± 0.036	2.771 ± 0.050
$0.10 < z \leqslant 0.12$	1.641 ± 0.025	-1.629 ± 0.027	4.860 ± 0.033	3.004 ± 0.038	2.754 ± 0.044
$0.12 < z \leqslant 0.14$	1.582 ± 0.022	-1.578 ± 0.023	4.807 ± 0.031	2.954 ± 0.029	2.797 ± 0.035
$0.14 < z \leqslant 0.16$	1.653 ± 0.024	-1.572 ± 0.025	4.785 ± 0.029	3.011 ± 0.028	2.796 ± 0.036
$0.16 < z \leqslant 0.18$	1.646 ± 0.023	-1.556 ± 0.022	4.751 ± 0.024	2.988 ± 0.025	2.768 ± 0.034
$0.18 < z \leqslant 0.20$	1.655 ± 0.025	-1.432 ± 0.023	4.787 ± 0.025	2.980 ± 0.026	2.783 ± 0.033
$0.20 < z \leqslant 0.22$	1.725 ± 0.027	-1.396 ± 0.024	4.732 ± 0.027	2.945 ± 0.026	2.834 ± 0.033
$0.22 < z \leqslant 0.24$	1.693 ± 0.022	-1.458 ± 0.023	4.696 ± 0.023	2.904 ± 0.023	2.736 ± 0.031
$0.24 < z \leqslant 0.26$	1.680 ± 0.022	-1.342 ± 0.026	4.719 ± 0.024	2.986 ± 0.026	2.667 ± 0.032
$0.26 < z \leqslant 0.28$	1.731 ± 0.026	-1.282 ± 0.033	4.652 ± 0.030	2.916 ± 0.029	2.712 ± 0.038
$0.28 < z \leqslant 0.30$	1.755 ± 0.030	-1.210 ± 0.041	4.627 ± 0.032	2.962 ± 0.035	2.763 ± 0.050
$0.30 < z \leqslant 0.32$	1.832 ± 0.027	-1.134 ± 0.043	4.516 ± 0.033	2.884 ± 0.039	2.655 ± 0.048
$0.32 < z \leqslant 0.34$	1.775 ± 0.031	-1.165 ± 0.054	4.484 ± 0.045	2.900 ± 0.044	2.718 ± 0.055
$0.34 < z \leqslant 0.36$	1.871 ± 0.042	-0.982 ± 0.077	4.434 ± 0.057	2.864 ± 0.057	2.620 ± 0.079
$0.36 < z \leqslant 0.38$	1.875 ± 0.056	-0.999 ± 0.099	4.411 ± 0.080	2.926 ± 0.091	3.012 ± 0.146
$0.38 < z \leqslant 0.40$	1.852 ± 0.070	-0.762 ± 0.114	4.461 ± 0.109	2.815 ± 0.153	2.715 ± 0.175

Table C3. Fully Calibrated Line Strength Measurements for $290 < \sigma_v \leqslant 320 \mathrm{kms}^{-1}$ mass sample.

Redshift Interval	Hβ (Å)	HγF (Å)	Mg b (Å)	Fe5270 (Å)	Fe5335 (Å)
$0.02 < z \leqslant 0.04$	1.534 ± 0.073	-1.675 ± 0.074	5.055 ± 0.087	3.115 ± 0.103	2.771 ± 0.150
$0.04 < z \leqslant 0.06$	1.481 ± 0.082	-1.918 ± 0.088	5.160 ± 0.106	3.143 ± 0.121	3.107 ± 0.171
$0.06 < z \leqslant 0.08$	1.524 ± 0.044	-1.861 ± 0.048	5.197 ± 0.057	3.040 ± 0.065	2.971 ± 0.090
$0.08 < z \leqslant 0.10$	1.566 ± 0.042	-1.781 ± 0.047	5.008 ± 0.056	3.083 ± 0.063	2.961 ± 0.090
$0.10 < z \leqslant 0.12$	1.612 ± 0.036	-1.705 ± 0.040	5.058 ± 0.051	3.083 ± 0.057	2.899 ± 0.070
$0.12 < z \leqslant 0.14$	1.586 ± 0.030	-1.684 ± 0.033	4.963 ± 0.045	3.039 ± 0.041	2.871 ± 0.051
$0.14 < z \leqslant 0.16$	1.567 ± 0.029	-1.565 ± 0.030	5.016 ± 0.037	3.011 ± 0.035	2.808 ± 0.048
$0.16 < z \leqslant 0.18$	1.630 ± 0.031	-1.623 ± 0.031	4.935 ± 0.035	3.040 ± 0.036	2.840 ± 0.051
$0.18 < z \leqslant 0.20$	1.626 ± 0.029	-1.548 ± 0.027	4.997 ± 0.030	3.110 ± 0.032	2.843 ± 0.041
$0.20 < z \leqslant 0.22$	1.622 ± 0.029	-1.467 ± 0.026	4.943 ± 0.030	3.075 ± 0.029	2.851 ± 0.038
$0.22 < z \leqslant 0.24$	1.640 ± 0.025	-1.505 ± 0.026	4.896 ± 0.027	2.990 ± 0.027	2.746 ± 0.038
$0.24 < z \leqslant 0.26$	1.645 ± 0.024	-1.423 ± 0.028	4.845 ± 0.027	3.060 ± 0.029	2.799 ± 0.037
$0.26 < z \leqslant 0.28$	1.728 ± 0.026	-1.376 ± 0.033	4.913 ± 0.031	3.022 ± 0.029	2.799 ± 0.040
$0.28 < z \leqslant 0.30$	1.755 ± 0.027	-1.291 ± 0.037	4.735 ± 0.030	3.015 ± 0.031	2.803 ± 0.048
$0.30 < z \leqslant 0.32$	1.759 ± 0.029	-1.269 ± 0.045	4.733 ± 0.035	3.037 ± 0.042	2.796 ± 0.054
$0.32 < z \leqslant 0.34$	1.781 ± 0.031	-1.087 ± 0.052	4.635 ± 0.045	2.997 ± 0.044	2.629 ± 0.058
$0.34 < z \leqslant 0.36$	1.805 ± 0.044	-1.159 ± 0.080	4.546 ± 0.062	2.837 ± 0.060	2.847 ± 0.088
$0.36 < z \leqslant 0.38$	1.779 ± 0.047	-1.170 ± 0.082	4.457 ± 0.069	3.089 ± 0.077	2.533 ± 0.131
$0.38 < z \leqslant 0.40$	1.805 ± 0.062	-1.155 ± 0.100	4.577 ± 0.097	2.869 ± 0.136	2.557 ± 0.166

Table C4. Fully Calibrated Line Strength Measurements for $320 < \sigma_v \leqslant 350 \mathrm{kms}^{-1}$ mass sample.

Redshift Interval	Hβ (Å)	HγF (Å)	Mg b (Å)	Fe5270 (Å)	Fe5335 (Å)
$0.02 < z \leqslant 0.04$	1.406 ± 0.139	-1.820 ± 0.134	5.270 ± 0.170	3.314 ± 0.194	3.061 ± 0.287
$0.04 < z \leqslant 0.06$	1.484 ± 0.086	-1.893 ± 0.087	5.132 ± 0.109	3.197 ± 0.123	3.000 ± 0.185
$0.06 < z \leqslant 0.08$	1.481 ± 0.109	-1.717 ± 0.123	5.405 ± 0.148	3.316 ± 0.161	3.053 ± 0.239
$0.08 < z \leqslant 0.10$	1.518 ± 0.067	-1.895 ± 0.076	5.359 ± 0.094	3.064 ± 0.105	3.038 ± 0.151
$0.10 < z \leqslant 0.12$	1.662 ± 0.075	-1.794 ± 0.087	5.147 ± 0.113	3.107 ± 0.124	3.130 ± 0.157
$0.12 < z \leqslant 0.14$	1.504 ± 0.059	-1.658 ± 0.066	5.122 ± 0.094	3.133 ± 0.084	2.766 ± 0.110
$0.14 < z \leqslant 0.16$	1.658 ± 0.053	-1.673 ± 0.056	5.229 ± 0.070	3.126 ± 0.067	3.019 ± 0.095
$0.16 < z \leqslant 0.18$	1.651 ± 0.047	-1.713 ± 0.049	5.153 ± 0.056	3.100 ± 0.058	3.067 ± 0.084
$0.18 < z \leqslant 0.20$	1.649 ± 0.043	-1.591 ± 0.041	5.181 ± 0.048	3.131 ± 0.050	3.051 ± 0.068
$0.20 < z \leqslant 0.22$	1.603 ± 0.043	-1.544 ± 0.041	5.134 ± 0.047	3.157 ± 0.045	3.050 ± 0.063
$0.22 < z \leqslant 0.24$	1.647 ± 0.034	-1.558 ± 0.037	5.163 ± 0.040	3.097 ± 0.040	3.019 ± 0.058
$0.24 < z \leqslant 0.26$	1.599 ± 0.035	-1.451 ± 0.043	4.967 ± 0.044	3.143 ± 0.046	2.803 ± 0.061
$0.26 < z \leqslant 0.28$	1.702 ± 0.039	-1.549 ± 0.050	5.019 ± 0.049	3.094 ± 0.046	2.963 ± 0.066
$0.28 < z \leqslant 0.30$	1.726 ± 0.035	-1.363 ± 0.048	4.992 ± 0.041	3.106 ± 0.043	2.952 ± 0.066
$0.30 < z \leqslant 0.32$	1.742 ± 0.035	-1.419 ± 0.055	4.917 ± 0.046	3.067 ± 0.053	3.036 ± 0.071
$0.32 < z \leqslant 0.34$	1.816 ± 0.036	-1.237 ± 0.061	4.793 ± 0.055	3.002 ± 0.053	2.868 ± 0.072
$0.34 < z \leqslant 0.36$	1.768 ± 0.049	-1.256 ± 0.091	4.730 ± 0.072	2.942 ± 0.070	2.934 ± 0.104
$0.36 < z \leqslant 0.38$	1.712 ± 0.065	-1.130 ± 0.114	4.663 ± 0.100	2.998 ± 0.110	2.863 ± 0.194
$0.38 < z \leqslant 0.40$	1.782 ± 0.076	-0.919 ± 0.122	4.703 ± 0.127	2.756 ± 0.176	2.796 ± 0.212

APPENDIX D: DERIVED SSP PARAMETER DATA

We provide here the SSP parameters determined for each of the mass samples shown in Figure 6. Parameter estimates are determined from the posterior probability distribution described in Section 3 and Section 4. Briefly, each SSP parameter is estimated by determining the 16, 50 and 84 percentiles of posterior distribution after marginalising over the remaining two parameters. For Tables D1-D4 the posterior distribution has been obtained using uniform priors that span the full support of each of the KMT05 parameters, i.e. age (Gyr) $\sim \mathcal{U}(0.31, 18.2)$, [Z/H] $\sim \mathcal{U}(-1.0, 0.97)$, [$\alpha$/Fe] $\sim \mathcal{U}(-0.25, 0.73)$. For Table D5 the posterior distribution has been re-weighted, as described in Section 4, to account for Gaussian priors placed on [Z/H] and [α/Fe], in order to better constrain the age–redshift relationship.

Table D1. SSP parameter data for $230 < \sigma_v \leqslant 260\,\mathrm{km\,s^{-1}}$ mass sample using $H\gamma F$, Mg b , Fe5270, Fe5335.

Redshift Interval	Age (Gyr)	[Z/H]	[α/Fe]
$0.02 < z \leqslant 0.04$	$8.46^{+0.77}_{-0.78}$	$0.319^{+0.032}_{-0.035}$	$0.238^{+0.018}_{-0.018}$
$0.04 < z \leqslant 0.06$	$8.42^{+0.54}_{-0.52}$	$0.315^{+0.023}_{-0.024}$	$0.228^{+0.011}_{-0.011}$
$0.06 < z \leqslant 0.08$	$8.49^{+0.38}_{-0.39}$	$0.307^{+0.017}_{-0.017}$	$0.247^{+0.009}_{-0.008}$
$0.08 < z \leqslant 0.10$	$7.57^{+0.42}_{-0.38}$	$0.321^{+0.019}_{-0.019}$	$0.230^{+0.009}_{-0.009}$
$0.10 < z \leqslant 0.12$	$7.66^{+0.39}_{-0.38}$	$0.294^{+0.019}_{-0.019}$	$0.241^{+0.009}_{-0.009}$
$0.12 < z \leqslant 0.14$	$7.56^{+0.35}_{-0.33}$	$0.296^{+0.017}_{-0.016}$	$0.235^{+0.008}_{-0.008}$
$0.14 < z \leqslant 0.16$	$7.56^{+0.39}_{-0.39}$	$0.300^{+0.019}_{-0.018}$	$0.263^{+0.009}_{-0.009}$
$0.16 < z \leqslant 0.18$	$8.11^{+0.40}_{-0.45}$	$0.273^{+0.020}_{-0.018}$	$0.248^{+0.010}_{-0.010}$
$0.18 < z \leqslant 0.20$	$7.27^{+0.45}_{-0.42}$	$0.276^{+0.020}_{-0.020}$	$0.271^{+0.010}_{-0.009}$
$0.20 < z \leqslant 0.22$	$6.56^{+0.42}_{-0.39}$	$0.310^{+0.017}_{-0.019}$	$0.272^{+0.010}_{-0.010}$
$0.22 < z \leqslant 0.24$	$7.16^{+0.42}_{-0.41}$	$0.276^{+0.019}_{-0.018}$	$0.258^{+0.009}_{-0.009}$
$0.24 < z \leqslant 0.26$	$6.66^{+0.44}_{-0.41}$	$0.272^{+0.017}_{-0.018}$	$0.285^{+0.010}_{-0.010}$
$0.26 < z \leqslant 0.28$	$7.13^{+0.59}_{-0.52}$	$0.220^{+0.022}_{-0.023}$	$0.274^{+0.012}_{-0.012}$
$0.28 < z \leqslant 0.30$	$6.60^{+0.67}_{-0.58}$	$0.234^{+0.025}_{-0.028}$	$0.249^{+0.014}_{-0.014}$
$0.30 < z \leqslant 0.32$	$6.03^{+0.63}_{-0.51}$	$0.218^{+0.032}_{-0.028}$	$0.247^{+0.015}_{-0.015}$
$0.32 < z \leqslant 0.34$	$5.07^{+0.55}_{-0.47}$	$0.260^{+0.037}_{-0.039}$	$0.263^{+0.019}_{-0.019}$
$0.34 < z \leqslant 0.36$	$4.80^{+0.71}_{-0.61}$	$0.249^{+0.047}_{-0.051}$	$0.271^{+0.025}_{-0.025}$
$0.36 < z \leqslant 0.38$	$4.34^{+0.90}_{-0.75}$	$0.196^{+0.074}_{-0.075}$	$0.228^{+0.040}_{-0.040}$
$0.38 < z \leqslant 0.40$	$5.24^{+2.17}_{-1.78}$	$0.307^{+0.120}_{-0.116}$	$0.339^{+0.065}_{-0.064}$

Table D2. SSP parameter data for $260 < \sigma_v \leqslant 290\,\mathrm{km\,s^{-1}}$ mass sample using $H\gamma F$, Mg b , Fe5270, Fe5335.

Redshift Interval	Age (Gyr)	[Z/H]	[α/Fe]
$0.02 < z \leqslant 0.04$	$10.30^{+1.04}_{-1.00}$	$0.334^{+0.039}_{-0.047}$	$0.252^{+0.020}_{-0.020}$
$0.04 < z \leqslant 0.06$	$8.84^{+0.55}_{-0.53}$	$0.380^{+0.018}_{-0.019}$	$0.261^{+0.011}_{-0.012}$
$0.06 < z \leqslant 0.08$	$7.44^{+0.49}_{-0.47}$	$0.375^{+0.018}_{-0.018}$	$0.251^{+0.010}_{-0.011}$
$0.08 < z \leqslant 0.10$	$8.26^{+0.43}_{-0.49}$	$0.355^{+0.017}_{-0.017}$	$0.263^{+0.010}_{-0.010}$
$0.10 < z \leqslant 0.12$	$8.08^{+0.47}_{-0.45}$	$0.365^{+0.016}_{-0.016}$	$0.277^{+0.010}_{-0.010}$
$0.12 < z \leqslant 0.14$	$7.65^{+0.37}_{-0.36}$	$0.364^{+0.014}_{-0.014}$	$0.271^{+0.009}_{-0.008}$
$0.14 < z \leqslant 0.16$	$7.37^{+0.38}_{-0.36}$	$0.372^{+0.014}_{-0.014}$	$0.260^{+0.008}_{-0.008}$
$0.16 < z \leqslant 0.18$	$7.51^{+0.34}_{-0.34}$	$0.358^{+0.012}_{-0.014}$	$0.260^{+0.007}_{-0.007}$
$0.18 < z \leqslant 0.20$	$6.05^{+0.29}_{-0.27}$	$0.395^{+0.012}_{-0.011}$	$0.277^{+0.007}_{-0.007}$
$0.20 < z \leqslant 0.22$	$5.75^{+0.31}_{-0.25}$	$0.394^{+0.014}_{-0.014}$	$0.266^{+0.008}_{-0.008}$
$0.22 < z \leqslant 0.24$	$7.10^{+0.32}_{-0.31}$	$0.341^{+0.013}_{-0.014}$	$0.271^{+0.007}_{-0.007}$
$0.24 < z \leqslant 0.26$	$5.81^{+0.30}_{-0.25}$	$0.376^{+0.013}_{-0.013}$	$0.282^{+0.007}_{-0.007}$
$0.26 < z \leqslant 0.28$	$5.57^{+0.32}_{-0.29}$	$0.367^{+0.015}_{-0.016}$	$0.275^{+0.009}_{-0.008}$
$0.28 < z \leqslant 0.30$	$4.79^{+0.35}_{-0.34}$	$0.399^{+0.019}_{-0.019}$	$0.261^{+0.011}_{-0.010}$
$0.30 < z \leqslant 0.32$	$5.11^{+0.32}_{-0.34}$	$0.343^{+0.020}_{-0.022}$	$0.267^{+0.011}_{-0.011}$
$0.32 < z \leqslant 0.34$	$5.13^{+0.40}_{-0.41}$	$0.344^{+0.026}_{-0.027}$	$0.248^{+0.014}_{-0.014}$
$0.34 < z \leqslant 0.36$	$4.52^{+0.50}_{-0.51}$	$0.338^{+0.033}_{-0.036}$	$0.265^{+0.018}_{-0.018}$
$0.36 < z \leqslant 0.38$	$3.43^{+0.71}_{-0.58}$	$0.438^{+0.072}_{-0.060}$	$0.206^{+0.027}_{-0.026}$
$0.38 < z \leqslant 0.40$	$3.34^{+0.83}_{-0.66}$	$0.399^{+0.095}_{-0.078}$	$0.280^{+0.039}_{-0.038}$

Table D3. SSP parameter data for $290 < \sigma_v \leqslant 320 \,\mathrm{km\,s^{-1}}$ mass sample using HγF, Mg b , Fe5270, Fe5335.

Redshift Interval	Age (Gyr)	[Z/H]	[α/Fe]
$0.02 < z \leqslant 0.04$	$7.43^{+1.35}_{-1.28}$	$0.420^{+0.049}_{-0.048}$	$0.294^{+0.028}_{-0.027}$
$0.04 < z \leqslant 0.06$	$8.19^{+1.69}_{-1.67}$	$0.458^{+0.065}_{-0.062}$	$0.253^{+0.031}_{-0.033}$
$0.06 < z \leqslant 0.08$	$8.73^{+0.89}_{-0.84}$	$0.435^{+0.031}_{-0.032}$	$0.293^{+0.018}_{-0.017}$
$0.08 < z \leqslant 0.10$	$8.07^{+0.78}_{-0.82}$	$0.421^{+0.031}_{-0.028}$	$0.259^{+0.017}_{-0.017}$
$0.10 < z \leqslant 0.12$	$7.36^{+0.68}_{-0.68}$	$0.439^{+0.027}_{-0.026}$	$0.282^{+0.015}_{-0.015}$
$0.12 < z \leqslant 0.14$	$7.72^{+0.52}_{-0.53}$	$0.408^{+0.020}_{-0.019}$	$0.274^{+0.012}_{-0.012}$
$0.14 < z \leqslant 0.16$	$6.66^{+0.46}_{-0.48}$	$0.431^{+0.017}_{-0.017}$	$0.305^{+0.010}_{-0.010}$
$0.16 < z \leqslant 0.18$	$7.21^{+0.50}_{-0.48}$	$0.411^{+0.018}_{-0.019}$	$0.277^{+0.010}_{-0.011}$
$0.18 < z \leqslant 0.20$	$5.88^{+0.40}_{-0.35}$	$0.460^{+0.017}_{-0.016}$	$0.288^{+0.008}_{-0.009}$
$0.20 < z \leqslant 0.22$	$5.35^{+0.32}_{-0.31}$	$0.464^{+0.015}_{-0.015}$	$0.284^{+0.009}_{-0.008}$
$0.22 < z \leqslant 0.24$	$6.69^{+0.36}_{-0.39}$	$0.400^{+0.013}_{-0.013}$	$0.296^{+0.008}_{-0.008}$
$0.24 < z \leqslant 0.26$	$5.45^{+0.31}_{-0.30}$	$0.434^{+0.015}_{-0.015}$	$0.277^{+0.009}_{-0.008}$
$0.26 < z \leqslant 0.28$	$5.07^{+0.34}_{-0.35}$	$0.455^{+0.017}_{-0.016}$	$0.297^{+0.009}_{-0.009}$
$0.28 < z \leqslant 0.30$	$4.82^{+0.34}_{-0.34}$	$0.428^{+0.018}_{-0.018}$	$0.267^{+0.009}_{-0.010}$
$0.30 < z \leqslant 0.32$	$4.62^{+0.41}_{-0.38}$	$0.436^{+0.021}_{-0.022}$	$0.265^{+0.011}_{-0.011}$
$0.32 < z \leqslant 0.34$	$4.32^{+0.41}_{-0.38}$	$0.404^{+0.024}_{-0.022}$	$0.282^{+0.014}_{-0.014}$
$0.34 < z \leqslant 0.36$	$4.79^{+0.69}_{-0.61}$	$0.374^{+0.035}_{-0.039}$	$0.253^{+0.019}_{-0.020}$
$0.36 < z \leqslant 0.38$	$5.27^{+0.80}_{-0.71}$	$0.323^{+0.049}_{-0.052}$	$0.244^{+0.025}_{-0.025}$
$0.38 < z \leqslant 0.40$	$5.74^{+1.23}_{-1.00}$	$0.297^{+0.068}_{-0.066}$	$0.296^{+0.037}_{-0.036}$

Table D4. SSP parameter data for $320 < \sigma_v \leqslant 350 \,\mathrm{km\,s^{-1}}$ mass sample using HγF, Mg b , Fe5270, Fe5335.

Redshift Interval	Age (Gyr)	[Z/H]	[α/Fe]
$0.02 < z \leqslant 0.04$	$6.37^{+2.54}_{-2.06}$	$0.525^{+0.094}_{-0.100}$	$0.272^{+0.051}_{-0.049}$
$0.04 < z \leqslant 0.06$	$8.25^{+1.83}_{-1.66}$	$0.446^{+0.066}_{-0.066}$	$0.256^{+0.034}_{-0.034}$
$0.06 < z \leqslant 0.08$	$5.16^{+2.00}_{-1.71}$	$0.577^{+0.100}_{-0.080}$	$0.308^{+0.041}_{-0.042}$
$0.08 < z \leqslant 0.10$	$8.23^{+1.56}_{-1.49}$	$0.479^{+0.058}_{-0.059}$	$0.310^{+0.027}_{-0.028}$
$0.10 < z \leqslant 0.12$	$6.78^{+1.50}_{-1.46}$	$0.490^{+0.061}_{-0.059}$	$0.261^{+0.032}_{-0.031}$
$0.12 < z \leqslant 0.14$	$7.01^{+1.08}_{-1.07}$	$0.446^{+0.043}_{-0.041}$	$0.307^{+0.026}_{-0.026}$
$0.14 < z \leqslant 0.16$	$5.72^{+0.96}_{-0.90}$	$0.526^{+0.039}_{-0.038}$	$0.299^{+0.020}_{-0.019}$
$0.16 < z \leqslant 0.18$	$6.25^{+0.83}_{-0.78}$	$0.502^{+0.033}_{-0.030}$	$0.279^{+0.016}_{-0.016}$
$0.18 < z \leqslant 0.20$	$4.78^{+0.61}_{-0.56}$	$0.550^{+0.028}_{-0.028}$	$0.293^{+0.013}_{-0.014}$
$0.20 < z \leqslant 0.22$	$4.37^{+0.53}_{-0.44}$	$0.558^{+0.025}_{-0.026}$	$0.283^{+0.013}_{-0.013}$
$0.22 < z \leqslant 0.24$	$4.81^{+0.52}_{-0.49}$	$0.540^{+0.024}_{-0.024}$	$0.299^{+0.012}_{-0.012}$
$0.24 < z \leqslant 0.26$	$5.09^{+0.52}_{-0.49}$	$0.476^{+0.025}_{-0.025}$	$0.288^{+0.013}_{-0.013}$
$0.26 < z \leqslant 0.28$	$5.38^{+0.67}_{-0.60}$	$0.489^{+0.028}_{-0.028}$	$0.278^{+0.014}_{-0.014}$
$0.28 < z \leqslant 0.30$	$3.96^{+0.46}_{-0.38}$	$0.530^{+0.037}_{-0.026}$	$0.285^{+0.013}_{-0.013}$
$0.30 < z \leqslant 0.32$	$4.36^{+0.57}_{-0.48}$	$0.505^{+0.029}_{-0.028}$	$0.260^{+0.014}_{-0.014}$
$0.32 < z \leqslant 0.34$	$4.21^{+0.53}_{-0.47}$	$0.462^{+0.032}_{-0.029}$	$0.275^{+0.016}_{-0.016}$
$0.34 < z \leqslant 0.36$	$4.50^{+0.79}_{-0.71}$	$0.439^{+0.043}_{-0.040}$	$0.259^{+0.022}_{-0.022}$
$0.36 < z \leqslant 0.38$	$3.98^{+1.04}_{-0.87}$	$0.435^{+0.087}_{-0.065}$	$0.258^{+0.035}_{-0.034}$
$0.38 < z \leqslant 0.40$	$3.58^{+1.16}_{-0.87}$	$0.425^{+0.114}_{-0.088}$	$0.319^{+0.046}_{-0.041}$

This paper has been typeset from a TeX/ LaTeX file prepared by the author.

Table D5. SSP ages determined for all mass samples using $H\gamma F$, $Mg\,b$, Fe5270, Fe5335 and using Gaussian priors on $[Z/H]$ and $[\alpha/Fe]$.

Redshift Interval	Age (Gyr) $230< \sigma_v \leqslant 260$	Age (Gyr) $260< \sigma_v \leqslant 290$	Age (Gyr) $290< \sigma_v \leqslant 320$	Age (Gyr) $320< \sigma_v \leqslant 350$
$0.02 < z \leqslant 0.04$	$9.15^{+0.35}_{-0.39}$	$9.71^{+0.31}_{-0.40}$	$7.33^{+0.61}_{-0.57}$	$6.79^{+0.76}_{-1.03}$
$0.04 < z \leqslant 0.06$	$9.05^{+0.32}_{-0.27}$	$9.27^{+0.25}_{-0.25}$	$9.14^{+0.55}_{-0.59}$	$6.84^{+0.71}_{-0.64}$
$0.06 < z \leqslant 0.08$	$8.86^{+0.22}_{-0.22}$	$7.74^{+0.21}_{-0.26}$	$8.92^{+0.34}_{-0.37}$	$6.76^{+0.79}_{-0.78}$
$0.08 < z \leqslant 0.10$	$8.28^{+0.19}_{-0.24}$	$8.04^{+0.26}_{-0.19}$	$7.99^{+0.34}_{-0.30}$	$7.39^{+0.53}_{-0.63}$
$0.10 < z \leqslant 0.12$	$7.85^{+0.22}_{-0.23}$	$8.08^{+0.28}_{-0.24}$	$7.62^{+0.31}_{-0.30}$	$6.39^{+0.65}_{-0.66}$
$0.12 < z \leqslant 0.14$	$7.80^{+0.20}_{-0.21}$	$7.63^{+0.20}_{-0.21}$	$7.29^{+0.24}_{-0.25}$	$5.57^{+0.51}_{-0.45}$
$0.14 < z \leqslant 0.16$	$7.77^{+0.23}_{-0.23}$	$7.54^{+0.22}_{-0.21}$	$6.63^{+0.23}_{-0.23}$	$5.94^{+0.44}_{-0.44}$
$0.16 < z \leqslant 0.18$	$7.94^{+0.23}_{-0.27}$	$7.37^{+0.20}_{-0.18}$	$6.84^{+0.23}_{-0.25}$	$5.99^{+0.40}_{-0.36}$
$0.18 < z \leqslant 0.20$	$7.07^{+0.26}_{-0.23}$	$6.60^{+0.14}_{-0.15}$	$6.49^{+0.28}_{-0.28}$	$5.36^{+0.30}_{-0.32}$
$0.20 < z \leqslant 0.22$	$6.94^{+0.27}_{-0.27}$	$6.29^{+0.21}_{-0.20}$	$5.92^{+0.13}_{-0.16}$	$5.08^{+0.29}_{-0.30}$
$0.22 < z \leqslant 0.24$	$6.99^{+0.25}_{-0.25}$	$6.66^{+0.21}_{-0.20}$	$6.04^{+0.17}_{-0.18}$	$5.17^{+0.28}_{-0.24}$
$0.24 < z \leqslant 0.26$	$6.38^{+0.23}_{-0.16}$	$5.99^{+0.17}_{-0.17}$	$5.52^{+0.18}_{-0.15}$	$4.48^{+0.25}_{-0.23}$
$0.26 < z \leqslant 0.28$	$5.91^{+0.37}_{-0.25}$	$5.60^{+0.17}_{-0.15}$	$5.48^{+0.20}_{-0.18}$	$4.92^{+0.30}_{-0.30}$
$0.28 < z \leqslant 0.30$	$5.80^{+0.26}_{-0.26}$	$5.38^{+0.16}_{-0.19}$	$4.82^{+0.17}_{-0.15}$	$4.18^{+0.24}_{-0.22}$
$0.30 < z \leqslant 0.32$	$5.21^{+0.26}_{-0.20}$	$4.83^{+0.19}_{-0.16}$	$4.73^{+0.20}_{-0.19}$	$4.23^{+0.28}_{-0.17}$
$0.32 < z \leqslant 0.34$	$4.80^{+0.25}_{-0.25}$	$4.91^{+0.20}_{-0.17}$	$4.01^{+0.17}_{-0.15}$	$3.62^{+0.16}_{-0.15}$
$0.34 < z \leqslant 0.36$	$4.43^{+0.32}_{-0.31}$	$4.23^{+0.28}_{-0.23}$	$3.91^{+0.33}_{-0.19}$	$3.48^{+0.19}_{-0.14}$
$0.36 < z \leqslant 0.38$	$3.59^{+0.36}_{-0.29}$	$4.47^{+0.19}_{-0.10}$	$3.56^{+0.38}_{-0.11}$	$3.25^{+0.25}_{-0.22}$
$0.38 < z \leqslant 0.40$	$5.98^{+0.84}_{-1.01}$	$3.92^{+0.25}_{-0.31}$	$4.03^{+0.37}_{-0.30}$	$2.91^{+0.30}_{-0.19}$